

Earthquake rupture on multiple splay faults and its effect on tsunamis

I. van Zelst^{1,2,3}, L. Rannabauer⁴, A.-A. Gabriel^{5,6}, Y. van Dinther^{1,7}

¹Seismology and Wave Physics, Institute of Geophysics, Department of Earth Sciences, ETH Zürich, Zürich, Switzerland

²Institute of Geophysics and Tectonics, School of Earth and Environment, University of Leeds, Leeds, LS2 9JT, United Kingdom

³Institute of Planetary Research, German Aerospace Center (DLR), Berlin, Germany

⁴Department of Informatics, Technical University of Munich, Munich, Germany

⁵Geophysics, Department of Earth and Environmental Sciences, LMU Munich, Munich, Germany

⁶Institute of Geophysics and Planetary Physics, Scripps Institution of Oceanography, University of California, La Jolla, CA, USA

⁷Department of Earth Sciences, Utrecht University, Utrecht, The Netherlands

Key Points:

- Multiple splay faults can be activated during a single earthquake by megathrust slip and dynamic stress transfer due to trapped waves
- Splay fault activation is facilitated by their favourable orientation with respect to the local stress field and their closeness to failure
- Long-term geodynamic stresses and fault geometries affect dynamic splay fault rupture and the subsequent tsunami

Corresponding author: Iris van Zelst, iris.vanzelst@dlr.de / iris.v.zelst@gmail.com

Abstract

Detailed imaging of accretionary wedges reveals splay fault networks that could pose a significant tsunami hazard. However, the dynamics of multiple splay fault activation during megathrust earthquakes and the consequent effects on tsunami generation are not well understood. We use a 2-D dynamic rupture model with complex topo-bathymetry and six curved splay fault geometries constrained from realistic tectonic loading modelled by a geodynamic seismic cycle model with consistent initial stress and strength conditions. We find that all splay faults rupture coseismically. While the largest splay fault slips due to a complex rupture branching process from the megathrust, all other splay faults are activated either top down or bottom up by dynamic stress transfer induced by trapped seismic waves. We ascribe these differences to local non-optimal fault orientations and variable along-dip strength excess. Generally, rupture on splay faults is facilitated by their favourable stress orientations and low strength excess as a result of high pore-fluid pressures. The ensuing tsunami modelled with non-linear 1-D shallow water equations consists of one high-amplitude crest related to rupture on the longest splay fault and a second broader wave packet resulting from slip on the other faults. This results in two episodes of flooding and a larger run-up distance than the single long-wavelength (300 km) tsunami sourced by the megathrust-only rupture. Since splay fault activation is determined by both variable stress and strength conditions and dynamic activation, considering both tectonic and earthquake processes is relevant for understanding tsunami-genesis.

Plain Language Summary

In subduction zones, where one tectonic plate moves beneath another, earthquakes can occur on many different faults. Splay faults are relatively steep faults that branch off the largest fault (the megathrust) in a subduction zone. As they are steeper than the megathrust, the same amount of movement on them could result in more vertical displacement of the seafloor. Therefore, splay faults are thought to play an important role in the generation of tsunamis. Here, we use computer simulations to study if an earthquake can break multiple splay faults at once and how this affects the resulting tsunami. We find that multiple splay faults can indeed fail during a single earthquake due to the stress changes from trapped seismic waves, which promote rupture on splay faults. Rupture on splay faults results in larger seafloor displacements with smaller wavelengths, so

53 the ensuing tsunami is bigger and results in two main flooding episodes at the coast. Our
54 results show that it is important to consider rupture on splay faults when assessing tsunami
55 hazard.

56 1 Introduction

57 Splay faults branch off the megathrust in the accretionary wedge or overriding plate
58 (e.g., Plafker, 1965; Fukao, 1979; Park et al., 2002). Observations of accretionary wedges
59 in subduction zones show multiple splay faults with a range of sizes and dips, although
60 not all of them are expected to be seismically active simultaneously (G. F. Moore et al.,
61 2001; Kimura et al., 2007; Kopp, 2013; Fabbri et al., 2020; Hananto et al., 2020). Earth-
62 quake ruptures originating on the megathrust can potentially activate splay faults. Apart
63 from complicating rupture dynamics, this may lead to important ramifications for tsunami-
64 genesis, as rupture on splay faults could increase the efficiency of tsunami generation (e.g.,
65 Fukao, 1979; Lotto et al., 2019; Hananto et al., 2020). Several studies suggested that splay
66 fault rupture played an important role in large tsunamigenic megathrust earthquakes,
67 such as the 2004 M_w 9.1–9.3 Sumatra-Andaman and 2010 M_w 8.0 Maule earthquakes
68 (DeDontney & Rice, 2012; Melnick et al., 2012; Waldhauser et al., 2012). Tsunami earth-
69 quakes in which the observed tsunami is larger than expected from surface wave mag-
70 nitude analysis of the earthquake (e.g., Kanamori, 1972; Heidarzadeh, 2011), such as the
71 365 Crete, 1946 Nankai, and 1964 Alaska earthquakes, have also been linked to splay fault
72 rupture (e.g., Cummins & Kaneda, 2000; Cummins et al., 2001; Shaw et al., 2008; Chap-
73 man et al., 2014; Haeussler et al., 2015; von Huene et al., 2016; Fan et al., 2017; Mar-
74 tin et al., 2019; Hananto et al., 2020; Suleimani & Freymueller, 2020).

75 Dynamic rupture modeling is a useful tool to understand the role of splay faults
76 in rupture dynamics (e.g., Kame et al., 2003; Wendt et al., 2009; Geist & Oglesby, 2009;
77 DeDontney et al., 2011; Tamura & Ide, 2011; DeDontney & Hubbard, 2012; Lotto et al.,
78 2019; Aslam et al., 2021). These studies show that parameters such as the initial stress,
79 branching angle, frictional properties, strength of the accretionary wedge, and material
80 contrasts along the megathrust affect splay fault rupture. Several coupled models have
81 been employed to solve for splay fault rupture dynamics and tsunamis sequentially or
82 simultaneously (Wendt et al., 2009; Geist & Oglesby, 2009; S. Li et al., 2014; Lotto et
83 al., 2019; Ulrich et al., 2022).

84 Dynamic rupture models of branching faults typically use simple, planar fault ge-
85 ometries, even if observed splay fault geometries are more complicated (e.g, Park et al.,
86 2002; G. Moore et al., 2007; Collot et al., 2008). Besides that, most dynamic rupture stud-
87 ies include only a single splay fault, which is partly necessitated by the difficulty of mod-
88 eling fault junctions with numerical methods (e.g., Aochi et al., 2002; DeDontney et al.,
89 2012; Pelties et al., 2014). Another reason for using predominantly simple fault geome-
90 tries in dynamic rupture modeling up to now is the difficulty in constraining consistent
91 initial stress and strength conditions on complex fault geometries. However, recent stud-
92 ies (Van Zelst et al., 2019; E. Madden et al., 2020; Wirp et al., 2021) have shown that
93 initial conditions for 2-D and 3-D megathrust dynamic rupture earthquake simulations
94 can be constrained from 2-D geodynamic long-term subduction and seismic cycle mod-
95 els. Indeed, this approach provides self-consistent initial fault loading stresses and fric-
96 tional strength, fault geometry, and material properties on and surrounding the megath-
97 rust, as well as consistency with crustal, lithospheric, and mantle deformation over ge-
98 ological time scales.

99 To understand the effect of multiple splay fault rupture with non-planar geome-
100 tries and subduction-initialised stress and strength on the free surface displacements and
101 the ensuing tsunami, we model dynamic rupture constrained by a geodynamic model of
102 long-term subduction and the subsequent tsunami propagation and inundation.

103 **2 Modeling approach**

104 We use the modeling approach presented in Van Zelst et al. (2019), where a geo-
105 dynamic seismic cycle (SC) model is used to constrain the initial conditions of a dynamic
106 rupture (DR) model. We extend this approach by using the resulting surface displace-
107 ments of the DR model as input for a tsunami propagation and inundation (TS) model.
108 Our modeling framework accounts for the varying temporal and spatial scales from geo-
109 dynamics to tsunami inundation (see also E. Madden et al., 2020). We apply this frame-
110 work to understand the dynamics of splay fault rupture by including six splay fault ge-
111 ometries constrained by the SC model within the DR model setup.

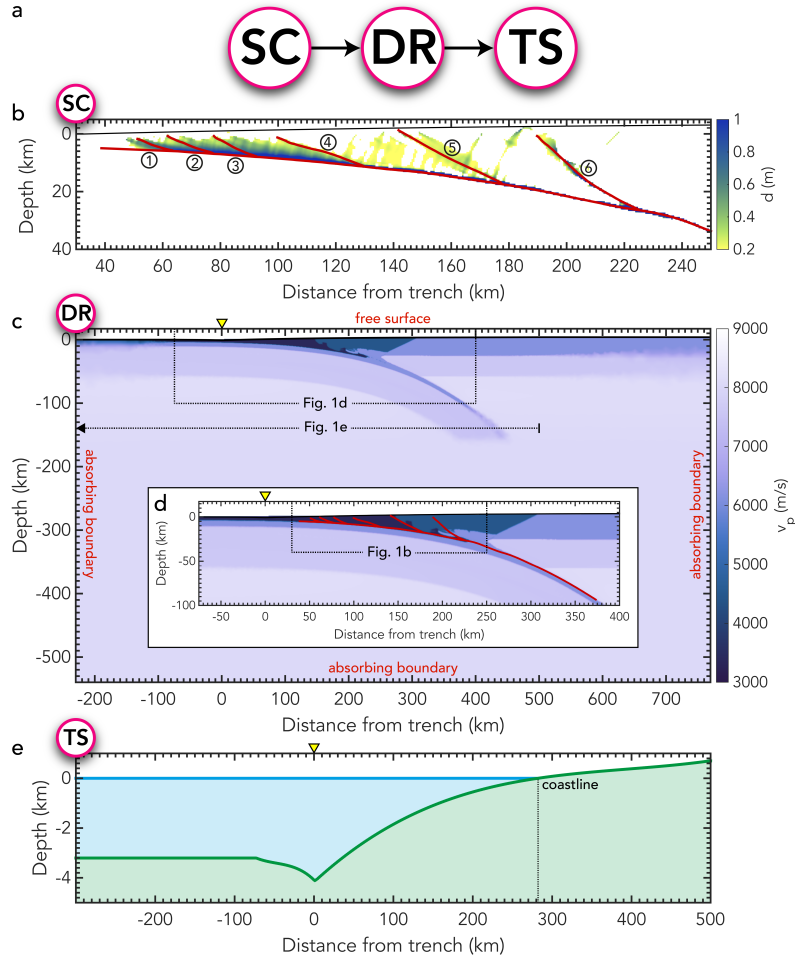


Figure 1. (a) Concept of the modeling approach: the output (i.e., fault geometry, lithological structure, material stress and strength) of a chosen slip event in the geodynamic seismic cycle (SC) model is used as input for the dynamic rupture (DR) model. The resulting surface displacements of the DR model are used as input for the tsunami propagation and inundation (TS) model. (b) Accumulated slip d in the sedimentary wedge after the SC slip event from Van Zyl et al. (2019). Picked splay fault geometries (red) are numbered for easy reference. Complete (c) and zoomed (d) model setup of the DR model with P -wave velocity v_p (see Van Zyl et al. (2019) for S -wave velocities), boundary conditions (red) and megathrust and splay fault geometries. (e) Model setup of the tsunami propagation and inundation model with the SC bathymetry (green) and initial sea surface height (blue). The coastline is located at $x = 282.25$ km. Note that the x -axis differs for each panel depending on the model setup size (trench indicated by the yellow triangle). Also note that the SC model has positive z -axis down, whereas the other two models have positive z -axis up.

2.1 Geodynamic seismic cycle model

We use the same SC model as Van Zelst et al. (2019) which is based on the Southern Chilean subduction zone. We use the output of the SC model as input for the DR model for one event. The SC model solves for the conservation of mass, momentum, and energy with a visco-elasto-plastic rheology (Gerya & Yuen, 2007). It models 4 million years of subduction followed by a seismic cycle phase with a 5-year time step with spontaneous slip events driven by a strongly rate-dependent friction (van Dinther, Gerya, Dalguer, Corbi, et al., 2013) using the seismo-thermo-mechanical (STM) modeling approach (van Dinther, Gerya, Dalguer, Mai, et al., 2013). For a full description and discussion of the methods, we refer the reader to Van Zelst et al. (2019).

We observe widespread visco-plastic shear bands in the sedimentary wedge in the SC model forming during megathrust slip events, which we interpret as faults (Figure 1b). Both in- and out-of-sequence thrusting fault geometries that are typically observed in nature (e.g., Kimura et al., 2007) are present.

For one slip event, we use the output of the SC model as input for the DR model according to Van Zelst et al. (2019). We pick six splay fault geometries according to the highest accumulated visco-plastic strain during the event visualised as the accumulated visco-plastic slip in Figure 1b (see Appendix A for details; Figures A1; S1-S6).

2.2 Dynamic rupture model

We use the two-dimensional version of the software package SeisSol (<http://www.seissol.org>) to model dynamic rupture in the model setup described by Van Zelst et al. (2019) with six additional splay fault geometries in the mesh (Figure 1c,d). Hence, all initial stresses, and the friction and material parametrisation of the dynamic rupture models are equivalent to the megathrust-only dynamic rupture models in (Van Zelst et al., 2019) (see section 3, therein). We model mode II along-dip rupture propagation (e.g., Ramos & Huang, 2019). SeisSol is based on an Arbitrary high-order accurate DERivative Discontinuous Galerkin method (ADER-DG, Dumbser and Käser (2006)) and uses unstructured tetrahedral meshes enabling geometrically complex models, such as branching and intersecting faults (de la Puente et al., 2009; Pelties et al., 2014). The on-fault element edge length is 200 m, which, combined with using basis functions of polynomial degree $p = 5$ (spatio-temporal order 6 numerical accuracy for wave propagation) results

143 in an effective resolution of 28.6 m through $(p+2)$ Gaussian integration points on the
 144 fault, which is sufficient to resolve the cohesive zone size (Day et al., 2005; Wollherr et
 145 al., 2018). At the top of the DR model setup, we employ a free surface boundary con-
 146 dition with topography derived from a 3rd order polynomial approximation of the rock-
 147 sticky air (Cramer et al., 2012) interface in the SC model from $x = -72.8$ km to $x = 499.6$ km,
 148 beyond which we assign constant topography values (Figure 1e). We run the model for
 149 180 s, which ensures smooth coupling to the TS model, as the surface displacements do
 150 not vary significantly after that time. To obtain the surface displacements of the DR model,
 151 we place 601 virtual seismometers from -100 km to 500 km at 5 m below the free sur-
 152 face with a spacing of 1 km to record the velocity field. To optimally capture the sur-
 153 face displacements, we place the seismometers within elements that have a free-surface
 154 boundary edge.

155 **2.3 Tsunami propagation and inundation model**

156 To model tsunami propagation, we solve the one-dimensional shallow water equa-
 157 tions, which consist of the conservation of mass and momentum and consider the hydro-
 158 static pressure caused by gravitational acceleration. Recently the more advanced Boussi-
 159 nesq equations have grown in popularity to model tsunami propagation (Spiegel & Vero-
 160 nis, 1960). However for models of the type that we simulate in this work (i.e., a large
 161 domain compared to a small wave amplitude) the shallow water equations have been val-
 162 idated and proven to be an accurate model (Carrier & Greenspan, 1958). To solve the
 163 non-linear shallow water equations, we employ a first order finite volume scheme (LeVeque
 164 et al., 2002) and we use a well-tested augmented Riemann solver to solve for inundation
 165 (George, 2008).

166 To incorporate dynamic surface displacements, we consider the bathymetry as a
 167 constant, defined by the unperturbed topography from the SC model, plus a time-dependent
 168 deformation from the DR model that incorporates all effects. Following Abrahams et al.
 169 (2020), this approach is sufficient to capture all components of the deformation that con-
 170 tribute to the tsunami. The constant topography from the SC model has an average beach
 171 angle of $7.2 \cdot 10^{-6}$ (Figure 1e). To compute the seafloor deformation from the DR model,
 172 we use the method by Tanioka and Satake (1996), which adds the vertical displacement
 173 to a linear approximation of the vertical contribution of the horizontal displacement. We
 174 then add the computed seafloor deformation displacements $\Delta b(x, t)$ from the DR model

175 to the SC model topography. The resulting displacement field contains fast travelling
 176 seismic waves, which are radiating from the earthquake source during the DR simula-
 177 tion. Waves are trapped within the sedimentary wedge between the uppermost part of
 178 the fault and the surface until the end of the simulation. To avoid imprinting of wave
 179 signals on the near-source seafloor deformation, we remove the seismic waves from all
 180 displacements used as tsunami sources. To this end, we apply a Fourier filter (Wirp et
 181 al., 2021) to the seafloor displacements which removes transient displacements result-
 182 ing from waves with a ratio of frequency over wave number higher than 300 m/s (Fig-
 183 ures S17-18).

184 At this point other approaches additionally account for the energy transfer from
 185 the seafloor to the water surface and apply a low pass filter to the horizontal displace-
 186 ment (Kajiura, 1970; Wendt et al., 2009). In our models the source size is relatively large
 187 compared to the source duration, so we follow Saito (2013) in ignoring this energy trans-
 188 fer and instead directly adapt the change of the seafloor to the sea-surface.

189 We consider a model domain from $x = -300$ km to $x = 500$ km, with the initial
 190 bathymetry from the SC model (Figure 1e). We set the coastline at $x = 282.25$ km to
 191 coincide with the downdip limit of the seismogenic zone (Klingelhoefer et al., 2010). This
 192 results in a maximum water depth of 4117 m. To discretise the model, we use 20,000 points,
 193 which translates to a uniform spacing of 40 m. We use adaptive time stepping and run
 194 the model for a total simulation time of 2 hours with maximum time steps of 0.5 s and
 195 minimum time steps of 0.08 s. The time step size is adapted according to the maximum
 196 wave speed in the model, which depends on the water column. Close to the coast, the
 197 size of the water column reduces to values close to zero, which increases the wave speeds
 198 and reduces the maximum admissible time step size according to the Courant-Friedrichs-
 199 Lewy condition (Courant et al., 1928). To avoid numerical instabilities, we consider cells
 200 with a water column of less than 10^{-6} m as dry.

201 **3 Results**

202 **3.1 Stress field and splay fault geometries**

203 The chosen six splay fault geometries that are activated during a representative slip
 204 event (Appendix A) result from realistic tectonic loading during retreating subduction
 205 on geodynamic time scales (Figure 1). The four shallowest splay faults (SF) 1-4 are lo-

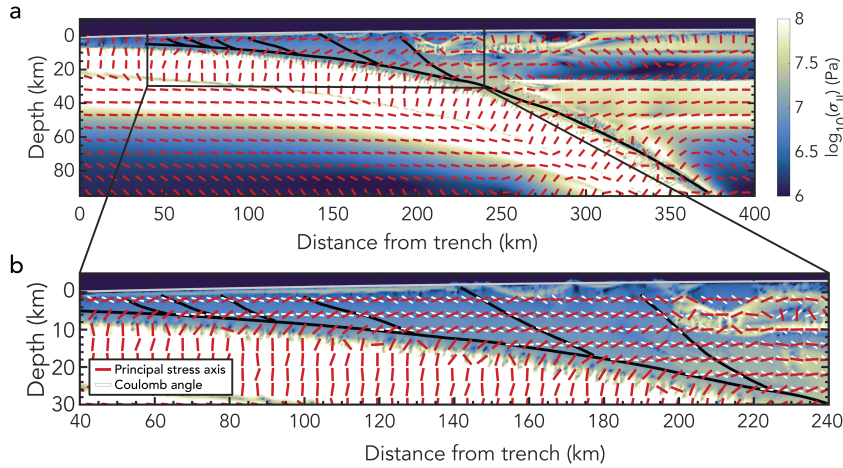


Figure 2. (a) Overview of the stress state at the start of the event in the SC model with (b) a zoom of the sedimentary wedge. The direction of the principal stress σ_1 is indicated by red bars. In (b) the white bars indicate the theoretical Coulomb angle at which faults form with respect to the principal stress direction in this compressional stress regime. The megathrust and splay fault geometries are indicated in black and the free surface geometry is indicated in light grey. Background colours show the variability of the stress magnitude through the second invariant of the deviatoric stress tensor.

206 cated within the sediments scrapped off from the ocean floor and SF5 follows the con-
 207 trast in shear modulus between the incoming sediments that make up the accretionary
 208 wedge and the sediments of the pre-existing sedimentary wedge (Figure 1d). At the branch-
 209 ing point with the megathrust, the largest splay fault (SF6) is initially situated in the
 210 weaker incoming sediments, but then travels through the stronger basalt and into the
 211 sedimentary wedge sediments. The dips of the splay faults average 24.0° and the branch
 212 angles between the splay faults and the megathrust average 14.4° (Table S1), which is
 213 in line with observations (Park et al., 2002) and Mohr-Coulomb theory.

214 At nucleation, the sedimentary and accretionary wedge are largely under compres-
 215 sion with the principal stress direction approximately 22° from horizontal (red bars in
 216 Figure 2). This agrees with dynamic coulomb wedge theory (Wang & Hu, 2006) as shown
 217 in van Dinther et al. (2014). Stress field variations are dominated by a depth-dependent,
 218 approximately linear stress increase (Figure 2b) following the pressure-dependence in the
 219 yield criterion. However, three different mechanisms lead to deviations from these gener-
 220 ally linearly increasing stresses. First, for SF6, sudden increases in stress and strength

221 are observed where the fault cuts through different rock types (Figures 3c; S7-S10, Van Zelst
 222 et al. (2019)). Second, frequent stress release due to megathrust ruptures affects the stresses
 223 in the deepest portion of the splay faults. Third, a sharp increase in strength along SF6
 224 results from a local absence of fluids and therefore a low pore-fluid pressure. The shal-
 225 low splay faults in the SC model are generally close to failure as indicated by a low strength
 226 excess of less than 1 MPa (Figures 3; S7-10). However, larger strength excess of 1-6 MPa
 227 exists across the large splay fault SF6 and the deeper parts of SF4 and SF5 (Figures 3;
 228 S7-10).

229 The likelihood of fault activation through earthquake rupture can be analysed through
 230 a comparison to theoretical fault growth angles (e.g., Kame et al., 2003). Faults form
 231 at an angle to the local stress field, which is generally believed to obey the Mohr-Coulomb
 232 failure criterion (e.g., Anderson, 1905; Sibson, 1994; Heidbach et al., 2018). We calcu-
 233 late the Coulomb angle α (white bars in Figure 2b) at which faults theoretically form
 234 with respect to the principal stress direction in a compressional stress regime according
 235 to (e.g., Wang & Hu, 2006; Kaus, 2010; Zang & Stephansson, 2010; Choi & Petersen,
 236 2015):

$$\alpha = -45^\circ + \frac{\phi}{2}, \quad (1)$$

237 where $\phi = \tan^{-1}(\mu_d)$ with μ_d being the dynamic friction coefficient of the sediments.
 238 We use the dynamic friction coefficient $\mu_d = 0.105$ to calculate the Coulomb angle in-
 239 stead of the static friction coefficient angle μ_s , since strain localisation forming shear bands
 240 in the SC model typically occurs during a slip event. Slip events are characterised by in-
 241 creased slip velocity and therefore reduced effective friction coefficient (Van Zelst et al.,
 242 2019). This results in a Coulomb angle of -42° with respect to the principal stresses.
 243 Throughout the sedimentary wedge, this leads to a Coulomb angle of approximately -20°
 244 with respect to the horizontal. The splay fault geometries generally align very well with
 245 the theoretical optimal faulting angles (Figure 2b), indicating that they are favourably
 246 orientated for activation during earthquake rupture. Interestingly, the deepest sections
 247 of SF1-3 and SF5, where they branch off the megathrust, are not aligned with the the-
 248oretical optimal Coulomb angles. Instead, the megathrust aligns with the Coulomb an-
 249-gle near the branching junctions.

250 During each slip event in the SC model, the entire accretionary wedge experiences
 251 large strains (Figures 1b, S1), resulting in repeated strain localisation on the same splay
 252 fault geometries. During the slip event, the amount of stress drop on the different splay
 253 faults is highly variable in the SC model (Figures 4, S11-S14). The largest splay fault
 254 SF6 shows stress drops up to 7.5 MPa in the basalt and sediments and an isolated large
 255 stress drop of 14.2 MPa in the accretionary wedge sediments (Figures 4c). SF5 gener-
 256 ally exhibits stress drops of 1-2 MPa, with the deepest part of the fault featuring stress
 257 drops up to 3.3 MPa (Figure S14). SF4 shows stress drops of 1-2 MPa near the branch-
 258 ing point. The shallow, small splay faults (SF1-3) do not experience any significant stress
 259 drop.

260 3.2 Dynamic earthquake rupture

261 We compare a model in which only the megathrust is allowed to rupture (Figure 5a,c;
 262 Van Zelst et al. (2019)) to the model in which the megathrust and the six splay faults
 263 are theoretically allowed to slip. The ruptures show similar rupture speeds, but differ-
 264 ent rupture duration with the model including splay faults rupturing for longer (89 s in-
 265 stead of 82 s). Slip differs significantly between the two ruptures with the model includ-
 266 ing splay faults exhibiting lower slip and slip velocities (Figure 5).

267 Earthquake rupture initiation is non-prescribed and solely driven by the initial con-
 268 ditions from the geodynamic seismic cycle model. After a two-stage nucleation at very
 269 low slip rates (a 4 s period of low rupture speed, followed by a 2 s high speed phase), spon-
 270 taneous rupture emerges on the megathrust ((1) in Figure 5b). Subsequently, rupture
 271 propagates both updip and downdip, where it is spontaneously arrested at the brittle-
 272 ductile transition (2) in both models (Figure 5a,b). In the updip direction, the main rup-
 273 ture front in the splay fault model encounters SF6 after 14.1 s. While the dynamic ac-
 274 tivation of SF6 appears to resemble rupture branching (DeDontney et al. (2011); Movie
 275 1, 2 in Supplementary Material), we observe a high degree of complexity on smaller scales.
 276 The passing megathrust rupture dynamically unclamps SF6, i.e., there is a decrease in
 277 the normal stress σ_n (Oglesby et al., 2008), which results in negligible slip over 1 km of
 278 the splay fault close to the fault junction without spontaneously propagating rupture.
 279 Subsequently the rupture jumps from the megathrust to SF6 due to dynamic trigger-
 280 ing, omitting the deepest 3 km of the splay fault that had a higher initial strength ex-
 281 cess (Figure 3), which only ruptures in a down-dip direction after 18 s ((3) in Figure 5j).

282 Unilateral dynamic rupture then propagates updip on the splay fault with slip veloci-
 283 ties of 4.7 m/s. Simultaneously, ahead of this rupture front, secondary ruptures are dy-
 284 namically triggered by the main megathrust rupture (4) leading to an apparently very
 285 high updip splay rupture speed. Behind this first, apparently fast splay rupture front,
 286 we observe fault reactivation due to multiple passing rupture fronts on the megathrust
 287 and free surface reflected seismic waves (5), resulting in a static slip maximum of 13.8 m.
 288 Due to the splay fault rupture, the slip velocities on the megathrust updip of the splay
 289 fault are sharply reduced compared to a model which only ruptures the megathrust. This
 290 leads to a slip discontinuity on the megathrust (Figure 5d).

291 The main rupture front on the megathrust passes SF5 without activating it (6),
 292 i.e., neither by branching nor dynamic triggering (Figure 5i). This difference in splay fault
 293 activation dynamics can be attributed to the local non-optimal orientation of SF5 near
 294 the branching junction, which forms an effective barrier for dynamic rupture propaga-
 295 tion. Instead, SF5 is activated at shallow depths of ~ 5 km at 32.8 s due to waves re-
 296 flecting from the free surface (7). Multiple rupture fronts then propagate downdip (i.e.,
 297 hosting reverse slip) on SF5, but the unfavourably oriented deepest 2.5 km of SF5 never
 298 fully ruptures (8). Since the passing of the primary megathrust rupture front does not
 299 trigger slip on SF5, there is no decrease in slip rate on the megathrust after it passes SF5.

300 Although the passing of the main rupture front induces small slip rates on SF1–
 301 4 on the order of ~ 0.02 m/s due to unclamping, they only rupture afterwards in a self-
 302 sustained manner at slip rates larger than 1 m/s due to static and dynamic stress changes.
 303 These are induced by secondary rupture front complexity on the megathrust as well as
 304 on SF5 and SF6 and multiple reflected (trapped) waves within the sedimentary wedge.
 305 The long rupture duration on these shallow splay faults leads to a maximum slip of 12.6 m
 306 for SF4 and 10.0 m, 8.1 m, and 8.0 m for SF1–3, respectively, barring some numerical
 307 outliers. Since slip occurs on the splay faults and the slip velocity on the megathrust is
 308 reduced when the rupture interacts with a splay fault, the maximum slip on the megath-
 309 rust in the model including splay fault rupture (48.9 m) is lower than in the model with-
 310 out splay fault rupture (57.6 m). The decrease in slip on the megathrust at the branch-
 311 ing points with the splay faults is visible as sharp discontinuities in Figure 5d, which con-
 312 tribute to the slip observed on the splay faults (Figure 5k-p). This indicates that slip
 313 is transferred from the megathrust onto the splay faults for SF1-4 and 6.

314 In summary, we find that all splay faults rupture coseismically, albeit in three dif-
315 ferent fashions. SF6 is unclamped by the primary rupture front, SF1-4 are dynamically
316 triggered by the reactivated megathrust, and SF5 slips near the surface due to dynamic
317 stress transfer from wave reflections from the free surface. We ascribe these differences
318 in fault activation to variable along-fault strength excess and fault orientation with re-
319 spect to the prevailing stress field. However, we generally observe that the splay faults
320 are favourably orientated with respect to the the stress field and have low strength ex-
321 cess resultant from high pore-fluid pressures.

322 The maximum stress drop, computed on-fault, on the megathrust on the order of
323 ~ 17 MPa is comparable in the models with and without splay faults (Figure S11, S15a,b).
324 Splay fault 6 shows the largest stress drop of all splay faults on the order of ~ 19 MPa
325 (Figures 4c and S15). The other splay faults show maximum stress drops of 2.5–6.5 MPa,
326 with the deeper splay faults exhibiting larger stress drops than the shallow splay faults
327 (Figures 4, S12-S15). In general, the stress drop is relatively constant along the splay
328 faults, with the exception of the branching point which typically shows a larger stress
329 drop than the rest of the splay fault. Splay fault 6 is the only splay fault which shows
330 varying stress drop along the fault with higher stress drops in the basalt and incoming
331 sediments directly below the basalt.

332 The model without splay faults has relatively uniform static vertical surface dis-
333 placements of ~ 5 m and a smooth profile of horizontal displacements of 47.8 m sea-
334 wards (Figure 6). In contrast, the model with splay faults shows clear vertical surface
335 displacement peaks corresponding to the shallow tips of the splay faults near the sur-
336 face (Figure 6b,c). The wavelengths of these peaks are ~ 80 – 95% smaller than the wave-
337 lengths of the vertical surface displacements due to rupture purely on the megathrust.
338 The largest peak of 9.3 m at 180 s is associated with SF6, whereas the other peaks with
339 amplitudes ranging from 4.7–6.5 m are associated with SF1–5. Hence, rupture on splay
340 faults increases the amplitude of the vertical displacements up to 86%. The amounts of
341 vertical displacement and slip are not linearly correlated (Figure S17) as other factors,
342 such as the dip angle and slip distribution on the fault also play a role. The effect of splay
343 fault rupture is less pronounced in the horizontal displacements with a 17% lower am-
344 plitude of the horizontal displacements compared to the model without splay faults (Fig-
345 ure 6d).

3.3 Tsunami propagation and inundation

The tsunami resulting from the model without splay faults consists of a single wave with a wavelength of 300 km and a maximum sea surface height of 6.5 m (Figure 7a). It arrives at the beach after 11 min and it takes a total of 74.5 min for the whole wave to arrive at the coast. There is one episode of flooding at the coast with a run-up distance of 1250 m. Here, we define run-up distance as a measure of how far inland the tsunami reaches horizontally compared to the original coastline (Satake, 2015).

In the model including six splay fault ruptures, the tsunami consists of one high wave crest corresponding to slip on SF6 ((7) in Figure 7b) and a broad wave packet resulting from slip on the other splay faults and shallow part of the megathrust ((1-6) in Figure 7b). Similar to the tsunami of the model without splay faults, the waves span a region of 300 km, but have smaller individual wavelengths. The tsunami first reaches the coast after 11 min and impacts the coast until 71.3 min. It reaches a maximum sea surface height of 12.2 m, which is almost double the height of the model without splay faults. Besides that, the flooding at the coast occurs in two episodes (Figure 8) in contrast to one flooding episode for the model without splay faults. The first episode is related to the large wave resultant from rupture on SF6, whereas the second episode relates to a wave originating from the interference of the smaller waves related to the other splay faults and shallow megathrust. The run-up distance of the tsunami is 2210 m, which is 77% larger than that of the tsunami sourced by a rupture without splay faults.

4 Discussion

Observational studies of accretionary wedges image multiple splay faults which pose a tsunami hazard (Kopp, 2013). It is difficult to assess if multiple splay faults rupture during a single earthquake and how that affects the ensuing tsunami. It is often assumed that only one splay fault at the time is seismically active in conjunction with the megathrust (e.g., Park et al., 2002; DeDontney & Hubbard, 2012). However, the uncertainty in tsunami source location (Sibuet et al., 2007; Waldhauser et al., 2012) and the exact locations of the ruptured fault planes could allow for multiple, closely-spaced (partially) ruptured splay faults during a single earthquake. Numerical models can shed light on the process of rupture on multiple splay faults, but initial fault stresses are difficult to constrain (e.g., Van Zelst et al., 2019) and the choice of numerical discretisation method

377 can hamper the geometric complexity of dynamic rupture models (e.g., DeDontney &
378 Hubbard, 2012). Here, we explicitly account for self-consistent initial fault stresses, com-
379 plex topo-bathymetry, and a shallowly dipping megathrust intersecting with six differ-
380 ent splay fault geometries. This linked framework including geodynamics, seismic cycles,
381 dynamic rupture and tsunami propagation and inundation allows us to address questions
382 about the viability and likelihood of splay fault ruptures and their impact on tsunami-
383 genesis.

384 It is currently unknown under what circumstances earthquakes will produce large
385 offsets of the seafloor, which is one cause of unexpectedly large tsunamis (e.g., Dunham
386 et al., 2020; Brodsky et al., 2021). Slip on the megathrust propagating onto splays through
387 dynamic or static stress changes has been inferred for past and recent tsunamigenic earth-
388 quakes (e.g., Fan et al., 2017; Cummins & Kaneda, 2000; Obana et al., 2017). Our re-
389 sults highlight that studying compound rupture of megathrusts and multiple or segmented
390 splay faults is important for the assessment of future hazardous events and to better un-
391 derstand the details of near-trench rupture processes that control seafloor uplift and hence
392 tsunami generation (Tanioka & Satake, 1996; Satake, 2015; Saito et al., 2019; E. Mad-
393 den et al., 2020; Wirp et al., 2021; Ulrich et al., 2022). Future efforts could aim to in-
394 clude region specific observations, such as high-resolution seismic imaging and geolog-
395 ical data in modeling workflows that link earthquake source models to tsunami models
396 to improve our understanding of tsunamis occurrence.

397 **4.1 Fault geometries**

398 One of the choices in our coupled modeling framework is the choice of fault geome-
399 tries in the SC model as input for the DR model. The chosen fault geometries determine
400 which stresses and strengths are ultimately used as input for the DR model, where the
401 initial stresses on the faults are crucial for the ensuing dynamic rupture.

402 The chosen megathrust geometry for this slip event is picked from the highest visco-
403 plastic strain rate during the event (Van Zelst et al., 2019). For all slip events in the SC
404 model, the megathrust is blind and follows the lithology contrast between the basaltic
405 oceanic crust and the incoming sediments below the sedimentary wedge. The megath-
406 rust is consistently located at that location, because it is the location of the largest dif-
407 ferential strain build-up and thus largest interseismic stressing rates. The incoming sed-

408 iments do not completely subduct together with the slab, as parts are also accreted to
409 the accretionary wedge (Cloos & Shreve, 1988; Von Huene & Scholl, 1991; Clift & Van-
410 nucchi, 2004). A blind, or buried, megathrust is thought to be less common in nature,
411 but has been inferred for e.g., the Cascadia subduction zone where no evidence of the
412 megathrust breaching the seafloor has been found (e.g., Flueh et al., 1998; Lotto et al.,
413 2019). Coupled earthquake-tsunami models by Lotto et al. (2019) show that the tsunami
414 profile resulting from a buried megathrust rupture with simple loading and strength prop-
415 erties is complex. Many small peaks and troughs are caused by the effect of enhanced
416 shallow slip and the vertical seafloor displacement, which we also observe in our model
417 (Figure 6).

418 Similar to the megathrust geometry, all six splay fault geometries considered here
419 are blind with the tip of the splay faults located at 2 km depth on average. This results
420 in more gradual, and hence less discontinuous surface displacements compared to stud-
421 ies where splay faults breach the seafloor (e.g., S. Li et al., 2014; Ulrich et al., 2022). In
422 addition, the surface displacements resulting from rupture on blind faults could also have
423 different, and specifically smaller, amplitudes that might affect tsunami height. However,
424 the surface displacements typically associated with interactions between the rupture and
425 the free surface typically have lower wavelengths (Nielsen, 1998) that are not thought
426 to have a strong effect on the tsunami (Saito et al., 2019). Therefore, we hypothesise that
427 the use of blind faults in this work does not affect our main conclusions.

428 The splay fault geometries do not significantly change between slip events in the
429 SC model and we observe no stress drop on SF1-3 during events in the SC model (Fig-
430 ures 4; S12-14), although strain localises and slip occurs on them. We do observe a stress
431 drop in the SC model on the larger splay faults of up to 7 MPa. However, in the DR mod-
432 els, we observe significantly more stress drop on each of the splay faults (Figures 4; S12-
433 14). This indicates the importance of the coupled modeling framework, where the DR
434 model fully resolves the ruptures, resulting in stress drops on the ruptured faults and
435 incorporating dynamic waves effects. These latter effects in particular have been shown
436 to be important for seismic cycle models (Thomas et al., 2014; Van Zelst et al., 2019).
437 We speculate that the repeated reactivation of the same splay fault geometries in the SC
438 model over each seismic cycle might not occur if two-way coupling of the codes were to
439 be employed such that the resulting stress state after the dynamic rupture would be fed
440 back into the SC model. The reason for this is that the stresses on the splay faults would

441 be reduced further after rupture due to larger dynamic stress drops, such that subsequent
 442 interseismic periods start with lower stresses that then would need to be increased slowly
 443 and steadily before the faults rupture again. Since the build-up of stress mostly occurs
 444 near the downdip limit of the seismogenic zone below which ductile creep leads to dif-
 445 ferential displacements, stresses would first need to be transferred updip to the splay fault
 446 locations (see e.g., Herrendörfer et al., 2015; Kammer et al., 2015; Dal Zilio et al., 2019).
 447 Reloading the splay faults for activation may thus take a significant amount of time.

448 4.2 Rupture on splay faults

449 Our models show that all six splay faults rupture when we use the self-consistent
 450 initial conditions from the SC model. This is partially due to the orientation of the splay
 451 faults with respect to the local stress field, which is generally favourable for rupture ac-
 452 cording to Coulomb theory (Figure 2b) (e.g., Wang & Hu, 2006; Kaus, 2010). The splay
 453 faults also exhibit low strength excess, particularly at shallow depths, (Figures 3;S7-S10)
 454 indicating that they are close to failure at the start of the rupture (e.g., S. Li et al., 2014).
 455 Here, we define strength excess as $\sigma_{\text{yield}}^{\text{dr}} - \tau$, where $\sigma_{\text{yield}}^{\text{dr}}$ is the fault yield stress and
 456 τ is the initial shear stress. The low strength excess of the shallow splay faults can largely
 457 be explained by the low strength of sediments in the sedimentary wedge due to the pres-
 458 ence of fluids and prevalent high pore-fluid pressures (van Dinther et al., 2014). Here,
 459 we assume high a pore-fluid pressure ratio $\frac{P_f}{P_s}$ of 0.95. This results in reasonable recur-
 460 rence intervals on seismic cycle time scales, while allowing for subduction along a shal-
 461 low megathrust on geodynamic time scales (van Dinther, Gerya, Dalguer, Mai, et al., 2013).
 462 In addition, 3-D dynamic rupture simulations (E. H. Madden et al., 2022) support the
 463 presence of high coseismic pore fluid pressure at megathrusts (Audet et al., 2009; To-
 464 bin & Saffer, 2009; Saffer & Tobin, 2011). The deeper splay faults SF4–6 are not as close
 465 to failure as the shallower splay faults, but still rupture due to the overall energetic rup-
 466 ture and wave reflections and the resulting stress changes. SF5 in particular does not
 467 rupture at the branching point due to the large strength excess and a high branching an-
 468 gles (21.8°) that misaligns SF5 with respect to the local stress field. Instead, it is acti-
 469 vated at shallow depths due to reflecting waves from the free surface where the strength
 470 excess on the fault is small. Hence, our results suggest that multiple splay faults rup-
 471 ture during an energetic event with reflecting waves when (1) they are favourably ori-
 472 entated with respect to the local stress field for rupture, i.e., they are strong faults ac-

473 cording to Andersonian faulting theory, and (2) they have a low strength excess, i.e., they
474 are close to failure.

475 Slip on our simulated 1-D splay faults is on the order of ~ 10 m. In nature, slip
476 on splay faults is generally hard to observe, but Chapman et al. (2014) report an esti-
477 mate of 3 m slip on a splay fault during the 1964 Alaska earthquake. Similarly, Cummins
478 and Kaneda (2000) infer up to 3.5 m splay fault slip during the 1946 Nankai earthquake.
479 In recent 3D dynamic rupture models of the 2004 Sumatra-Andaman earthquake, three
480 co-seismically activated large-scale splay faults host larger slip on the order of 6-8 m (Ulrich
481 et al., 2022). Additionally, another, shorter splay fault near the trench with a steeper
482 dip hosts up to 10s of meters of slip in these models. While observational estimates of
483 splay fault slip are lower than our simulated slip, the modeled vertical surface displace-
484 ments do align with those typically associated with splay faults. For example, Suito and
485 Freymueller (2009); Suleimani and Freymueller (2020) report 10 m of vertical surface up-
486 lift for the splay fault rupture of the 1964 Alaska earthquake.

487 The relatively high geodynamically constrained 2D dynamic rupture fault slip can
488 be reduced (Van Zelst et al., 2019) by simulating rupture in three dimensions, as illus-
489 trated in M. Li et al. (2021) for a strike-slip setting and E. Madden et al. (2020); Wirp
490 et al. (2021) for a subduction zone setting, where the stresses and strengths are adapted
491 to avoid unilateral nucleation along the 2D fault and thereby reduce fault slip. The 3D
492 megathrust dynamic rupture models in (Wirp et al., 2021) additionally use a constant,
493 not geodynamically informed, characteristic slip distance, which further reduces the amount
494 of slip. We expect that considering off-fault plasticity would further decrease shallow fault
495 slip on the megathrust and splay faults Ulrich et al. (2022). Future studies could use these
496 findings to expand on the approach presented in this manuscript to obtain more real-
497 istic slip values on splay faults. Since our models are restricted to two dimensions and
498 show a relatively large amount of slip on the splay faults, we caution that our models
499 may overestimate the absolute tsunami heights and run-up distance.

500 **4.3 Tsunamis resulting from rupture on splay faults**

501 In the tsunami models, the effect of slip on splay faults is visible in the propagat-
502 ing wave and the inundation pattern at the coast (Figures 7,8; Goda et al. (2014)). The
503 tsunami model without splay fault rupture also shows localised crests (Figure 7a), al-

504 though to a lesser extent. This indicates that crests in the tsunami data cannot exclu-
505 sively be contributed to splay fault rupture. Similarly, the absence of complexity in the
506 tsunami data, particularly with regards to the second wave packet, does not necessar-
507 ily mean that rupture only occurred on one splay fault. Indeed, the effect of rupture on
508 other, smaller splay faults might not be distinguishable based on tsunami data alone.
509 To relate our findings directly to tsunami data, the here found splay fault effects should
510 be analysed with more complex bathymetry and 3-D complexity in future studies (Matsuyama
511 et al., 1999; Bletery et al., 2015; Ulrich et al., 2019; Tonini et al., 2020). Recent stud-
512 ies using a similar methodology to the one presented here have already attempted this
513 for megathrust-only events (E. Madden et al., 2020; Wirp et al., 2021). However, one
514 of the major limitations in these 3-D studies is the uncertainties in how to accurately
515 account for any lateral variation in the initial stresses and strengths on the megathrust
516 since the considered geodynamic seismic cycle model is two-dimensional. This limita-
517 tion is enhanced when complex splay fault geometries are considered in addition to the
518 megathrust. Lastly, the here used hydrostatic shallow-water-based tsunami modeling ap-
519 proach does not fully capture smaller-scale complexity during tsunami genesis nor dis-
520 persive effects during tsunami wave propagation, and future studies may extend our ap-
521 proach to account for a nonlinear hydrodynamic response (Kim et al., 2017; Saito et al.,
522 2019), corrections for dispersive Earth elasticity, and non-dispersive water compressibil-
523 ity (Tsai et al., 2013) or fully coupled seismic, acoustic, and gravity modeling (Lotto et
524 al., 2019; Krenz et al., 2021).

525 **5 Conclusions**

526 We develop and use a novel modeling framework that combines geodynamics, seis-
527 mic cycles, dynamic rupture, and tsunami generation, propagation, and inundation to
528 understand the rupture dynamics and tsunamigenesis of multiple splay faults. This linked
529 framework constrains the geometry, stress, and strength of the megathrust, six splay faults
530 and the surrounding rocks in a physically self-consistent manner. To first order the on-
531 fault stresses of splay faults increase linearly with depth. However, deviations occur due
532 to variations in lithology, pore fluid pressure and deep stress release. In our geodynamic
533 seismic cycle model, we analyse theoretical fault growth angles with respect to the prin-
534 cipal stress direction assuming a Coulomb angle in a compressional stress regime. We
535 find that large portions of most splay faults are favourably orientated, aiding activation

536 during megathrust earthquake rupture. In addition, the splay faults generally have low
537 strength excess due to high pore fluid pressures in large parts of the sedimentary wedge,
538 indicating that they are close to failure.

539 We find that all splay faults are dynamically activated by various mechanisms in
540 the dynamic earthquake rupture model, such as the passing of the megathrust rupture
541 front and stress changes from reflected waves in the sedimentary wedge. We observe rup-
542 ture branching from the megathrust to the largest splay fault, and detail the small-scale
543 dynamic fault interactions of unclamping and rupture jumping. The main rupture front
544 on the megathrust passes all other splay faults without activating them by branching.
545 We attribute this difference in splay fault activation dynamics to local variations in strength
546 excess and non-optimal orientations of all shorter splays near the branching junction,
547 which forms an effective barrier for dynamic rupture propagation. The second largest
548 splay, SF5, is slipping only partially and in down-dip reverse manner due to waves re-
549 flecting from the free surface. While the passing of the main rupture front unclamps the
550 four shorter splays SF1-4, they rupture delayed due to static and dynamic stress changes
551 from megathrust rupture complexity and slip on the respectively larger splays. Even-
552 tually, all splay faults experience slip reactivation during the same earthquake simula-
553 tion due to stress changes induced by multiple reflected (trapped) waves within the sed-
554 imentary wedge.

555 Rupture on the largest splay fault results in a local, short-wavelength increase in
556 tsunami height. A second, broad wave packet in the tsunami is due to slip on multiple
557 splay faults and the shallow megathrust. This wave packet is similar in width to the one
558 produced in the model with a pure megathrust rupture, albeit with larger amplitude and
559 shorter wavelength wave crests relating to the activation of each splay fault. However,
560 at the coast, the multiple wave crests can no longer be distinguished, making it difficult
561 to determine if multiple splay faults ruptured from tsunami data alone.

562 Our multi-physics models imply that simultaneous rupture on multiple splay faults
563 is mechanically viable and is facilitated by the low strength and favourable stress ori-
564 entation of the faults resulting from long-term tectonics and the strong dynamic (re-)activation
565 potential of splay faults. It is therefore important to take the possibility of rupture on
566 multiple splay faults into consideration in tsunami hazard.

Appendix A Defining splay fault geometries from the geodynamic seismic cycle model

To provide well-defined fault geometries as input to the DR model, we approximate the splay geometries in the sedimentary wedge by analysing the visco-plastic strain ε_{vp} visualised as the accumulated visco-plastic slip $d = 2\Delta x \cdot \varepsilon_{vp}$ in Figure 1b with $\Delta x = 500$ m representing the fault width (van Dinther, Gerya, Dalguer, Mai, et al., 2013). We calculate ε_{vp} from the second invariant of the visco-plastic strain rate $\dot{\varepsilon}_{vp,II} = \sqrt{\dot{\varepsilon}_{vp,xx}^2 + \dot{\varepsilon}_{vp,xz}^2}$ according to

$$\varepsilon_{vp} = \Delta t \sum_{t=1}^{t_{max}} \dot{\varepsilon}_{vp,II,t}, \quad (\text{A1})$$

where $t = 0$ is the coupling time step for which the output of the SC model is used as input for the DR model according to Van Zelst et al. (2019). Δt is the time step (5 years) of the SC model, and t_{max} is the final time step of the coupled SC event. We verified that the viscous component in the visco-plastic strain rate is negligible (Van Zelst et al., 2019), such that $\dot{\varepsilon}_{vp,II}$ shows the effect of plastic rock behaviour.

To pick discrete splay fault geometries from the visco-plastic strain distribution in the SC model (Figure S1), we only consider regions where the minimum slip is 0.16 m (Figure 1b). This corresponds to a strain rate of 10^{-12} s^{-1} . This threshold highlights the regions of strain during the event, and hence the splay fault geometries. We then pick six representative splay fault geometries (Figure 1b). We show the complete procedure for picking each splay fault in Figure A1 for splay fault 6 (see Figures S2-6 for the other splay faults). For each splay fault, we manually determine the x -extent of the fault. x_{min} is initially determined by visual inspection of Figure 1b, which is then iteratively adjusted based on the highest strain. We choose an arbitrarily large value of x_{max} , which is later adjusted based on meshing requirements at the branching point between the splay fault and the megathrust. Then, for each nodal x -coordinate, we pick the z -coordinate with the highest strain in the sedimentary wedge, i.e., disregarding the megathrust at which the largest strain is accumulated (red dots in panel (a) of Figure A1). We manually reposition any outliers that clearly belong to adjacent faults to align with the observed strain localisation (red dots with cyan borders in panel (a) of Figure A1; see Figures S2-6).

We then smooth the fault geometry with a moving average low-pass filter scheme with a span of 25 points (red dots in panel (b) of Figure A1; Van Zelst et al., 2019). To

597 ensure that the splay faults connect to the megathrust in the most efficient manner for
598 the mesh, we limit the x -extent of the splay faults (red dots with yellow borders in panel
599 (b) of Figure A1). The final geometries of the splay faults are then shown in panel (c)
600 of Figures A1; S2-6. Details of the splay fault geometries are listed in Table S1 in the
601 supplementary material and the full geometry of the splay faults can be found in Data
602 Sets S1 to S6.

603 We do not connect the splay faults to the surface, because there is no indication
604 that they reach the surface in the geodynamic seismic cycle model (Figure A1). This is
605 due to the predefined decreased pore-fluid pressure ratio of 0.4 in the top kilometre of
606 the SC model. Hence, we only consider blind splay faults here. There are also fault ge-
607 ometries other than splay faults present in the yielding sedimentary wedge of the geo-
608 dynamic seismic cycle model, such as antithetic fault planes (Figures 1b; A1). However,
609 here we focus solely on the more conventional splay fault geometries and do not include
610 any antithetic fault geometries to limit the complexity of our model.

611 **Acknowledgements**

612 We would like to thank the Editor Satoshi Ide, the anonymous Associate Editor,
613 and two reviewers. From a previous submission to GRL, we would like to thank the Ed-
614 itor Germán Prieto, the Associate Editor Victor Tsai, reviewer Kenny Ryan, and an anony-
615 mous reviewer. Their feedback have greatly helped to shape and improve this work.

616 We warmly thank Stephanie Wollherr, Thomas Ulrich, Casper Pranger, Luca Dal
617 Zilio, and Andreas Fichtner for sharing their expertise on the SC and DR models with
618 us. We also thank the Tectonics Group at the University of Leeds for helpful comments
619 and discussion that improved this manuscript. We are much obliged to Sebastian Ret-
620 tenberger, who originally wrote the tsunami code.

621 We use scientific colour maps by Crameri (2018b) to prevent visual distortion of
622 the data and exclusion of readers with colour-vision deficiencies (Crameri, 2018a).

623 We used the computational resources of the ETH cluster Euler. This work was part
624 of the ASCETE-II project (Advanced Simulation of Coupled Earthquake-Tsunami Events)
625 funded by the Volkswagen Foundation grant 88479. Additionally, IvZ was funded by the
626 Royal Society (UK) through Research Fellows Enhancement Award RGF\EA\181084.
627 IvZ also acknowledges the financial support and endorsement from the DLR Manage-

628 ment Board Young Research Group Leader Program and the Executive Board Member
629 for Space Research and Technology. AAG acknowledges support from the European Unions
630 Horizon 2020 research and innovation programme (TEAR ERC Starting grant no. 852992;
631 ChEESE project, grant agreement No. 823844), the German Research Foundation (DFG)
632 (projects GA 2465/2-1, GA 2465/3-1) and the National Science Foundation (NSF, Grant
633 No. EAR-2121666).

634 **Author contribution statement**

635 IvZ conceived the study, designed and ran the SC and DR models, analysed the
636 results, and wrote the article. LR designed the tsunami models together with IvZ and
637 ran them. YvD and AAG supervised IvZ and contributed to the analysis of the SC and
638 DR models. All authors discussed the results and contributed to the final manuscript.

639 **Data availability statement**

640 We use the data of the geodynamic seismic cycle model provided in Van Zelst et
641 al. (2019) to set up our dynamic rupture model. The additional six splay fault geome-
642 tries can be found in the supplementary material of this article and will be uploaded to
643 Zenodo. We use the two-dimensional version of the open source software package Seis-
644 Sol to model dynamic rupture (<http://www.seissol.org>). We use the one-dimensional
645 version of the open source code SWE (shallow water equations) to model the tsunami
646 (<https://github.com/TUM-I5/SWE>), which will also be made available on Zenodo.

647 **References**

- 648 Abrahams, L. S., Dunham, E. M., Krenz, L., Saito, T., & Gabriel, A.-A. (2020).
649 Comparison of techniques for coupled earthquake and tsunami modeling. In
650 *Agu fall meeting abstracts* (Vol. 2020, pp. NH021–06).
- 651 Anderson, E. M. (1905). *The dynamics of faulting: Transactions of the edinburgh ge-*
652 *ological society viii, 1905, p387-402*. Edinburgh Geological Society.
- 653 Aochi, H., Madariaga, R., & Fukuyama, E. (2002). Effect of normal stress during
654 rupture propagation along nonplanar faults. *Journal of Geophysical Research:*
655 *Solid Earth, 107*(B2), ESE–5.
- 656 Aslam, K. S., Thomas, A. M., & Melgar, D. (2021). The effect of fore-arc deforma-
657 tion on shallow earthquake rupture behavior in the cascadia subduction zone.

- 658 *Geophysical Research Letters*, 48(20), e2021GL093941.
- 659 Audet, P., Bostock, M. G., Christensen, N. I., & Peacock, S. M. (2009). Seismic ev-
660 idence for overpressured subducted oceanic crust and megathrust fault sealing.
661 *Nature*, 457(7225), 76–78.
- 662 Bletery, Q., Sladen, A., Delouis, B., & Mattéo, L. (2015). Quantification of tsunami
663 bathymetry effect on finite fault slip inversion. *Pure and Applied Geophysics*,
664 172(12), 3655–3670.
- 665 Brodsky, E., Hilley, G., Roman, D., Tobin, H., & (RCN), S. R. C. N. (2021).
666 Draft SZ4D Implementation Plan - A New Initiative to Understand
667 Subduction Zone Geohazards. *SZ4D Research Coordination Network*.
668 Retrieved from [https://www.sz4d.org/{_}files/ugd/aa1820{_}](https://www.sz4d.org/{_}files/ugd/aa1820{_}6d126a5d461d4d09952f81d5fcf1f159.pdf)
669 [6d126a5d461d4d09952f81d5fcf1f159.pdf](https://www.sz4d.org/{_}files/ugd/aa1820{_}6d126a5d461d4d09952f81d5fcf1f159.pdf)
- 670 Carrier, G. F., & Greenspan, H. P. (1958). Water waves of finite ampli-
671 tude on a sloping beach. *Journal of Fluid Mechanics*, 4(1), 97109. doi:
672 10.1017/S0022112058000331
- 673 Chapman, J. B., Elliott, J., Doser, D. I., & Pavlis, T. L. (2014). Slip on the suckling
674 hills splay fault during the 1964 alaska earthquake. *Tectonophysics*, 637, 191–
675 197.
- 676 Choi, E., & Petersen, K. D. (2015). Making coulomb angle-oriented shear bands in
677 numerical tectonic models. *Tectonophysics*, 657, 94–101.
- 678 Clift, P., & Vannucchi, P. (2004). Controls on tectonic accretion versus erosion in
679 subduction zones: Implications for the origin and recycling of the continental
680 crust. *Reviews of Geophysics*, 42(2).
- 681 Cloos, M., & Shreve, R. L. (1988). Subduction-channel model of prism accretion,
682 melange formation, sediment subduction, and subduction erosion at convergent
683 plate margins: 1. background and description. *Pure and Applied Geophysics*,
684 128(3), 455–500.
- 685 Collot, J.-Y., Agudelo, W., Ribodetti, A., & Marcaillou, B. (2008). Origin of a
686 crustal splay fault and its relation to the seismogenic zone and underplating
687 at the erosional north ecuador–south colombia oceanic margin. *Journal of*
688 *Geophysical Research: Solid Earth*, 113(B12).
- 689 Courant, R., Friedrichs, K., & Lewy, H. (1928). Über die partiellen differenzengle-
690 ichungen der mathematischen physik. *Mathematische annalen*, 100(1), 32–74.

- 691 Cramer, F. (2018a). Geodynamic diagnostics, scientific visualisation and StagLab
692 3.0. *Geoscientific Model Development*, 11(6), 2541–2562.
- 693 Cramer, F. (2018b). *Scientific colour-maps*. Zenodo. Retrieved from [http://doi](http://doi.org/10.5281/zenodo.1243862)
694 [.org/10.5281/zenodo.1243862](http://doi.org/10.5281/zenodo.1243862) doi: <http://doi.org/10.5281/zenodo.1243862>
- 695 Cramer, F., Schmeling, H., Golabek, G. J., Duretz, T., Orendt, R., Buitert, S. J. H.,
696 ... Tackley, P. J. (2012). A comparison of numerical surface topography cal-
697 culations in geodynamic modelling: an evaluation of the ‘sticky air’ method.
698 *Geophysical Journal International*, 189(1), 38–54.
- 699 Cummins, P. R., Hori, T., & Kaneda, Y. (2001). Splay fault and megathrust earth-
700 quake slip in the Nankai trough. *Earth, planets and space*, 53(4), 243–248.
- 701 Cummins, P. R., & Kaneda, Y. (2000). Possible splay fault slip during the 1946
702 Nankai earthquake. *Geophysical Research Letters*, 27(17), 2725–2728.
- 703 Dal Zilio, L., van Dinther, Y., Gerya, T. V., & Avouac, J.-P. (2019). Bimodal seis-
704 micity in the Himalaya controlled by fault friction and geometry. *Nature com-*
705 *munications*, 10(1), 48.
- 706 Day, S. M., Dalguer, L. A., Lapusta, N., & Liu, Y. (2005). Comparison of finite
707 difference and boundary integral solutions to three-dimensional spontaneous
708 rupture. *Journal of Geophysical Research: Solid Earth*, 110(B12).
- 709 DeDontney, N., & Hubbard, J. (2012). Applying wedge theory to dynamic rupture
710 modeling of fault junctions. *Bulletin of the Seismological Society of America*,
711 102(4), 1693–1711.
- 712 DeDontney, N., & Rice, J. R. (2012). Tsunami wave analysis and possibility of splay
713 fault rupture during the 2004 Indian Ocean earthquake. *Pure and applied geo-*
714 *physics*, 169(10), 1707–1735.
- 715 DeDontney, N., Rice, J. R., & Dmowska, R. (2011). Influence of material contrast on
716 fault branching behavior. *Geophysical Research Letters*, 38(14).
- 717 DeDontney, N., Rice, J. R., & Dmowska, R. (2012). Finite element modeling of
718 branched ruptures including off-fault plasticity. *Bulletin of the Seismological*
719 *Society of America*, 102(2), 541–562.
- 720 de la Puente, J., Ampuero, J.-P., & Käser, M. (2009). Dynamic rupture modeling on
721 unstructured meshes using a discontinuous Galerkin method. *Journal of Geo-*
722 *physical Research: Solid Earth*, 114(B10).
- 723 Dumbser, M., & Käser, M. (2006). An arbitrary high-order discontinuous Galerkin

- 724 method for elastic waves on unstructured meshes-II. The three-dimensional
 725 isotropic case. *Geophysical Journal International*, *167*(1), 319–336.
- 726 Dunham, E. M., Thomas, A., Becker, T. W., Cattania, C., Hawthorne, J., Hubbard,
 727 J., ... Platt, J. (2020). Megathrust modeling workshop report. *EarthArXiv*.
 728 Retrieved from <https://doi.org/10.31223/X5730M> doi: 10.31223/X5730M
- 729 Fabbri, O., Goldsby, D., Chester, F., Karpoff, A., Morvan, G., Ujiie, K., ... others
 730 (2020). Deformation Structures From Splay and Décollement Faults in the
 731 Nankai Accretionary Prism, SW Japan (IODP NanTroSEIZE Expedition 316):
 732 Evidence for Slow and Rapid Slip in Fault Rocks. *Geochemistry, Geophysics,*
 733 *Geosystems*, *21*(6), e2019GC008786.
- 734 Fan, W., Bassett, D., Jiang, J., Shearer, P. M., & Ji, C. (2017). Rupture evolu-
 735 tion of the 2006 Java tsunami earthquake and the possible role of splay faults.
 736 *Tectonophysics*, *721*, 143–150.
- 737 Flueh, E. R., Fisher, M. A., Bialas, J., Childs, J. R., Klaeschen, D., Kukowski, N.,
 738 ... others (1998). New seismic images of the Cascadia subduction zone from
 739 cruise SO108ORWELL. *Tectonophysics*, *293*(1-2), 69–84.
- 740 Fukao, Y. (1979). Tsunami earthquakes and subduction processes near deep-sea
 741 trenches. *Journal of Geophysical Research: Solid Earth*, *84*(B5), 2303–2314.
- 742 Geist, E. L., & Oglesby, D. D. (2009). Tsunamis: Stochastic models of occurrence
 743 and generation mechanisms. In R. A. Meyers (Ed.), *Encyclopedia of complex-*
 744 *ity and systems science* (pp. 1–29). New York, NY: Springer New York. Re-
 745 trieved from https://doi.org/10.1007/978-3-642-27737-5_595-1 doi: 10
 746 .1007/978-3-642-27737-5_595-1
- 747 George, D. L. (2008). Augmented Riemann solvers for the shallow water equations
 748 over variable topography with steady states and inundation. *Journal of Com-*
 749 *putational Physics*, *227*(6), 3089–3113.
- 750 Gerya, T. V., & Yuen, D. A. (2007). Robust characteristics method for modelling
 751 multiphase visco-elasto-plastic thermo-mechanical problems. *Physics of the*
 752 *Earth and Planetary Interiors*, *163*(1), 83–105.
- 753 Goda, K., Mai, P. M., Yasuda, T., & Mori, N. (2014). Sensitivity of tsunami wave
 754 profiles and inundation simulations to earthquake slip and fault geometry for
 755 the 2011 Tohoku earthquake. *Earth, Planets and Space*, *66*(1), 105.
- 756 Haeussler, P. J., Armstrong, P. A., Liberty, L. M., Ferguson, K. M., Finn, S. P.,

- 757 Arkle, J. C., & Pratt, T. L. (2015). Focused exhumation along megathrust
758 splay faults in Prince William Sound, Alaska. *Quaternary Science Reviews*,
759 *113*, 8–22.
- 760 Hananto, N., Leclerc, F., Li, L., Etchebes, M., Carton, H., Tapponnier, P., ... Wei,
761 S. (2020). Tsunami earthquakes: Vertical pop-up expulsion at the forefront of
762 subduction megathrust. *Earth and Planetary Science Letters*, *538*, 116197.
- 763 Heidarzadeh, M. (2011). Major tsunami risks from splay faulting. *The Tsunami*
764 *Threat-Research and Technology*, 67–80.
- 765 Heidbach, O., Rajabi, M., Cui, X., Fuchs, K., Müller, B., Reinecker, J., ... others
766 (2018). The world stress map database release 2016: Crustal stress pattern
767 across scales. *Tectonophysics*, *744*, 484–498.
- 768 Herrendörfer, R., Van Dinther, Y., Gerya, T. V., & Dalguer, L. A. (2015). Earth-
769 quake supercycle in subduction zones controlled by the width of the seismo-
770 genic zone. *Nature Geoscience*, *8*(6), 471.
- 771 Kajiura, K. (1970). 45. tsunami source, energy and the directivity of wave radia-
772 tion.
- 773 Kame, N., Rice, J. R., & Dmowska, R. (2003). Effects of prestress state and rupture
774 velocity on dynamic fault branching. *Journal of Geophysical Research: Solid*
775 *Earth*, *108*(B5).
- 776 Kammer, D. S., Radiguet, M., Ampuero, J.-P., & Molinari, J.-F. (2015). Linear elas-
777 tic fracture mechanics predicts the propagation distance of frictional slip. *Tri-*
778 *bology letters*, *57*(3), 1–10.
- 779 Kanamori, H. (1972). Mechanism of tsunami earthquakes. *Physics of the earth and*
780 *planetary interiors*, *6*(5), 346–359.
- 781 Kaus, B. J. (2010). Factors that control the angle of shear bands in geodynamic nu-
782 merical models of brittle deformation. *Tectonophysics*, *484*(1-4), 36–47.
- 783 Kim, J., Pedersen, G. K., Løvholt, F., & LeVeque, R. J. (2017). A boussinesq type
784 extension of the geoclaw model—a study of wave breaking phenomena applying
785 dispersive long wave models. *Coastal engineering*, *122*, 75–86.
- 786 Kimura, G., Kitamura, Y., Hashimoto, Y., Yamaguchi, A., Shibata, T., Ujiie, K., &
787 Okamoto, S. (2007). Transition of accretionary wedge structures around the
788 up-dip limit of the seismogenic subduction zone. *Earth and Planetary Science*
789 *Letters*, *255*(3-4), 471–484.

- 790 Klingelhoefer, F., Gutscher, M.-A., Ladage, S., Dessa, J.-X., Graindorge, D., Franke,
791 D., ... Chauhan, A. (2010). Limits of the seismogenic zone in the epicentral
792 region of the 26 December 2004 great Sumatra-Andaman earthquake: Results
793 from seismic refraction and wide-angle reflection surveys and thermal model-
794 ing. *Journal of Geophysical Research: Solid Earth*, 115(B1).
- 795 Kopp, H. (2013). Invited review paper: The control of subduction zone structural
796 complexity and geometry on margin segmentation and seismicity. *Tectono-*
797 *physics*, 589, 1–16.
- 798 Krenz, L., Uphoff, C., Ulrich, T., Gabriel, A.-A., Abrahams, L. S., Dunham, E. M.,
799 & Bader, M. (2021). 3d acoustic-elastic coupling with gravity: the dynamics
800 of the 2018 palu, sulawesi earthquake and tsunامي. In *Proceedings of the inter-*
801 *national conference for high performance computing, networking, storage and*
802 *analysis* (pp. 1–14).
- 803 LeVeque, R. J., et al. (2002). *Finite volume methods for hyperbolic problems*
804 (Vol. 31). Cambridge university press.
- 805 Li, M., Pranger, C., & van Dinther, Y. (2021). Characteristics of earthquake cy-
806 cles: a cross-dimensional comparison of 1d to 3d simulations. *Earth and Space*
807 *Science Open Archive*, 50. Retrieved from [https://doi.org/10.1002/essoar](https://doi.org/10.1002/essoar.10509020.2)
808 [.10509020.2](https://doi.org/10.1002/essoar.10509020.2) doi: 10.1002/essoar.10509020.2
- 809 Li, S., Moreno, M., Rosenau, M., Melnick, D., & Oncken, O. (2014). Splay fault
810 triggering by great subduction earthquakes inferred from finite element models.
811 *Geophysical Research Letters*, 41(2), 385–391.
- 812 Lotto, G. C., Jeppson, T. N., & Dunham, E. M. (2019). Fully coupled simula-
813 tions of megathrust earthquakes and tsunamis in the Japan Trench, Nankai
814 Trough, and Cascadia Subduction Zone. *Pure and Applied Geophysics*, 176(9),
815 4009–4041.
- 816 Madden, E., Bader, M., Behrens, J., Van Dinther, Y., Gabriel, A.-A., Rannabauer,
817 L., ... Van Zelst, I. (2020). Linked 3-D modelling of megathrust earthquake-
818 tsunami events: from subduction to tsunami run up. *Geophysical Journal*
819 *International*, 224(1), 487–516.
- 820 Madden, E. H., Ulrich, T., & Gabriel, A.-A. (2022). The state of pore fluid pressure
821 and 3-d megathrust earthquake dynamics. *Journal of Geophysical Research:*
822 *Solid Earth*, 127(4), e2021JB023382.

- 823 Martin, S. S., Li, L., Okal, E. A., Morin, J., Tetteroo, A. E., Switzer, A. D., & Sieh,
824 K. E. (2019). Reassessment of the 1907 Sumatra tsunami earthquake based
825 on macroseismic, seismological, and tsunami observations, and modeling. *Pure
826 and Applied Geophysics*, *176*(7), 2831–2868.
- 827 Matsuyama, M., Walsh, J., & Yeh, H. (1999). The effect of bathymetry on tsunami
828 characteristics at Sisano Lagoon, Papua New Guinea. *Geophysical Research
829 Letters*, *26*(23), 3513–3516.
- 830 Melnick, D., Moreno, M., Motagh, M., Cisternas, M., & Wesson, R. L. (2012). Splay
831 fault slip during the Mw 8.8 2010 Maule Chile earthquake. *Geology*, *40*(3),
832 251–254.
- 833 Moore, G., Bangs, N., Taira, A., Kuramoto, S., Pangborn, E., & Tobin, H. (2007).
834 Three-dimensional splay fault geometry and implications for tsunami genera-
835 tion. *Science*, *318*(5853), 1128–1131.
- 836 Moore, G. F., Taira, A., Klaus, A., Becker, L., Boeckel, B., Cragg, B. A., ... others
837 (2001). New insights into deformation and fluid flow processes in the Nankai
838 Trough accretionary prism: Results of Ocean Drilling Program Leg 190. *Geo-
839 chemistry, Geophysics, Geosystems*, *2*(10).
- 840 Nielsen, S. B. (1998). Free surface effects on the propagation of dynamic rupture.
841 *Geophysical research letters*, *25*(1), 125–128.
- 842 Obana, K., Nakamura, Y., Fujie, G., Kodaira, S., Kaiho, Y., Yamamoto, Y., &
843 Miura, S. (2017, 12). Seismicity in the source areas of the 1896 and 1933 San-
844 rikyu earthquakes and implications for large near-trench earthquake faults.
845 *Geophysical Journal International*, *212*(3), 2061–2072. Retrieved from
846 <https://doi.org/10.1093/gji/ggx532> doi: 10.1093/gji/ggx532
- 847 Oglesby, D. D., Mai, P. M., Atakan, K., & Pucci, S. (2008). Dynamic models of
848 earthquakes on the North Anatolian fault zone under the Sea of Marmara:
849 Effect of hypocenter location. *Geophysical Research Letters*, *35*(18).
- 850 Park, J.-O., Tsuru, T., Kodaira, S., Cummins, P. R., & Kaneda, Y. (2002). Splay
851 fault branching along the Nankai subduction zone. *Science*, *297*(5584), 1157–
852 1160.
- 853 Pelties, C., Gabriel, A.-A., & Ampuero, J.-P. (2014). Verification of an ADER-DG
854 method for complex dynamic rupture problems. *Geoscientific Model Develop-
855 ment*, *7*(3), 847–866.

- 856 Plafker, G. (1965). Tectonic deformation associated with the 1964 Alaska earth-
857 quake. *Science*, *148*(3678), 1675–1687.
- 858 Ramos, M. D., & Huang, Y. (2019). How the transition region along the Cascadia
859 megathrust influences coseismic behavior: Insights from 2-D dynamic rupture
860 simulations. *Geophysical Research Letters*, *46*(4), 1973–1983.
- 861 Saffer, D. M., & Tobin, H. J. (2011). Hydrogeology and mechanics of subduction
862 zone forearcs: Fluid flow and pore pressure. *Annual Review of Earth and Plan-
863 etary Sciences*, *39*, 157–186.
- 864 Saito, T. (2013). Dynamic tsunami generation due to sea-bottom deformation:
865 Analytical representation based on linear potential theory. *Earth, Planets and
866 Space*, *65*(12), 1411–1423.
- 867 Saito, T., Baba, T., Inazu, D., Takemura, S., & Fukuyama, E. (2019). Synthe-
868 sizing sea surface height change including seismic waves and tsunami using a
869 dynamic rupture scenario of anticipated Nankai trough earthquakes. *Tectono-
870 physics*, 228166.
- 871 Satake, K. (2015). 4.19 - Tsunamis. In G. Schubert (Ed.), *Treatise on geo-
872 physics* (Second ed., p. 477 - 504). Oxford: Elsevier. Retrieved from [http://
873 www.sciencedirect.com/science/article/pii/B9780444538024000865](http://www.sciencedirect.com/science/article/pii/B9780444538024000865)
874 doi: <https://doi.org/10.1016/B978-0-444-53802-4.00086-5>
- 875 Shaw, B., Ambraseys, N., England, P., Floyd, M., Gorman, G., Higham, T., ... Pig-
876 gott, M. (2008). Eastern Mediterranean tectonics and tsunami hazard inferred
877 from the AD 365 earthquake. *Nature Geoscience*, *1*(4), 268–276.
- 878 Sibson, R. H. (1994). An assessment of field evidence for byerleefriction. *Pure and
879 Applied Geophysics*, *142*(3), 645–662.
- 880 Sibuet, J.-C., Rangin, C., Le Pichon, X., Singh, S., Cattaneo, A., Graindorge, D., ...
881 others (2007). 26th December 2004 great Sumatra–Andaman earthquake: Co-
882 seismic and post-seismic motions in northern Sumatra. *Earth and Planetary
883 Science Letters*, *263*(1-2), 88–103.
- 884 Spiegel, E. A., & Veronis, G. (1960). On the boussinesq approximation for a com-
885 pressible fluid. *The Astrophysical Journal*, *131*, 442.
- 886 Suito, H., & Freymueller, J. T. (2009). A viscoelastic and afterslip postseismic defor-
887 mation model for the 1964 alaska earthquake. *Journal of Geophysical Research:
888 Solid Earth*, *114*(B11).

- 889 Suleimani, E., & Freymueller, J. T. (2020). Near-field modeling of the 1964 Alaska
890 tsunami: the role of splay faults and horizontal displacements. *Journal of Geo-*
891 *physical Research: Solid Earth*, e2020JB019620.
- 892 Tamura, S., & Ide, S. (2011). Numerical study of splay faults in subduction zones:
893 The effects of bimaterial interface and free surface. *Journal of Geophysical Re-*
894 *search: Solid Earth*, 116(B10).
- 895 Tanioka, Y., & Satake, K. (1996). Tsunami generation by horizontal displacement of
896 ocean bottom. *Geophysical Research Letters*, 23(8), 861–864.
- 897 Thomas, M. Y., Lapusta, N., Noda, H., & Avouac, J.-P. (2014). Quasi-dynamic
898 versus fully dynamic simulations of earthquakes and aseismic slip with and
899 without enhanced coseismic weakening. *Journal of Geophysical Research: Solid*
900 *Earth*, 119(3), 1986–2004.
- 901 Tobin, H. J., & Saffer, D. M. (2009). Elevated fluid pressure and extreme mechanical
902 weakness of a plate boundary thrust, nankai trough subduction zone. *Geology*,
903 37(8), 679–682.
- 904 Tonini, R., Basili, R., Maesano, F. E., Tiberti, M. M., Lorito, S., Romano, F., ...
905 Volpe, M. (2020). Importance of earthquake rupture geometry on tsunami
906 modelling: the Calabrian Arc subduction interface (Italy) case study. *Geophys-*
907 *ical Journal International*, 223(3), 1805–1819.
- 908 Tsai, V. C., Ampuero, J.-P., Kanamori, H., & Stevenson, D. J. (2013). Estimating
909 the effect of earth elasticity and variable water density on tsunami speeds.
910 *Geophysical Research Letters*, 40(3), 492–496.
- 911 Ulrich, T., Gabriel, A.-A., & Madden, E. H. (2022). Stress, rigidity and sediment
912 strength control megathrust earthquake and tsunami dynamics. *Nature Geo-*
913 *science*, 1–7.
- 914 Ulrich, T., Vater, S., Madden, E. H., Behrens, J., van Dinther, Y., Van Zelst, I., ...
915 Gabriel, A.-A. (2019). Coupled, physics-based modeling reveals earthquake dis-
916 placements are critical to the 2018 Palu, Sulawesi Tsunami. *Pure and Applied*
917 *Geophysics*, 176(10), 4069–4109.
- 918 van Dinther, Y., Gerya, T. V., Dalguer, L. A., Corbi, F., Funicello, F., & Mai,
919 P. M. (2013). The seismic cycle at subduction thrusts: 2. Dynamic implica-
920 tions of geodynamic simulations validated with laboratory models. *Journal of*
921 *Geophysical Research: Solid Earth*, 118(4), 1502–1525.

- 922 van Dinther, Y., Gerya, T. V., Dalguer, L. A., Mai, P. M., Morra, G., & Giardini,
 923 D. (2013). The seismic cycle at subduction thrusts: Insights from seismo-
 924 thermo-mechanical models. *Journal of Geophysical Research: Solid Earth*,
 925 *118*(12), 6183–6202.
- 926 van Dinther, Y., Mai, P. M., Dalguer, L. A., & Gerya, T. V. (2014). Modeling the
 927 seismic cycle in subduction zones: The role and spatiotemporal occurrence of
 928 off-megathrust earthquakes. *Geophysical Research Letters*, *41*(4), 1194–1201.
- 929 Van Zelst, I., Wollherr, S., Gabriel, A.-A., Madden, E. H., & van Dinther, Y. (2019).
 930 Modeling megathrust earthquakes across scales: One-way coupling from geo-
 931 dynamics and seismic cycles to dynamic rupture. *Journal of Geophysical*
 932 *Research: Solid Earth*, *124*(11), 11414–11446.
- 933 von Huene, R., Miller, J. J., Klaeschen, D., & Dartnell, P. (2016). A possible source
 934 mechanism of the 1946 Unimak Alaska far-field tsunami: uplift of the mid-
 935 slope terrace above a splay fault zone. In *Global tsunami science: Past and*
 936 *future, volume i* (pp. 4189–4201). Springer.
- 937 Von Huene, R., & Scholl, D. W. (1991). Observations at convergent margins con-
 938 cerning sediment subduction, subduction erosion, and the growth of continen-
 939 tal crust. *Reviews of Geophysics*, *29*(3), 279–316.
- 940 Waldhauser, F., Schaff, D. P., Diehl, T., & Engdahl, E. R. (2012). Splay faults
 941 imaged by fluid-driven aftershocks of the 2004 Mw 9.2 Sumatra-Andaman
 942 earthquake. *Geology*, *40*(3), 243–246.
- 943 Wang, K., & Hu, Y. (2006). Accretionary prisms in subduction earthquake cy-
 944 cles: The theory of dynamic Coulomb wedge. *Journal of Geophysical Research:*
 945 *Solid Earth*, *111*(B6).
- 946 Wendt, J., Oglesby, D. D., & Geist, E. L. (2009). Tsunamis and splay fault dynam-
 947 ics. *Geophysical Research Letters*, *36*(15).
- 948 Wirp, S. A., Gabriel, A.-A., Schmeller, M., H Madden, E., van Zelst, I., Krenz, L.,
 949 ... Rannabauer, L. (2021). 3d linked subduction, dynamic rupture, tsunami,
 950 and inundation modeling: Dynamic effects of supershear and tsunami earth-
 951 quakes, hypocenter location, and shallow fault slip. *Frontiers in Earth Science*,
 952 *9*, 177.
- 953 Wollherr, S., Gabriel, A.-A., & Uphoff, C. (2018). Off-fault plasticity in three-
 954 dimensional dynamic rupture simulations using a modal Discontinuous

955 Galerkin method on unstructured meshes: Implementation, verification,
956 and application. *Geophysical Journal International*, 214, 1556–1584. doi:
957 <https://doi.org/10.1093/gji/ggy213>
958 Zang, A., & Stephansson, O. (2010). Rock fracture criteria. In *Stress field of the*
959 *earths crust* (pp. 37–62). Springer.

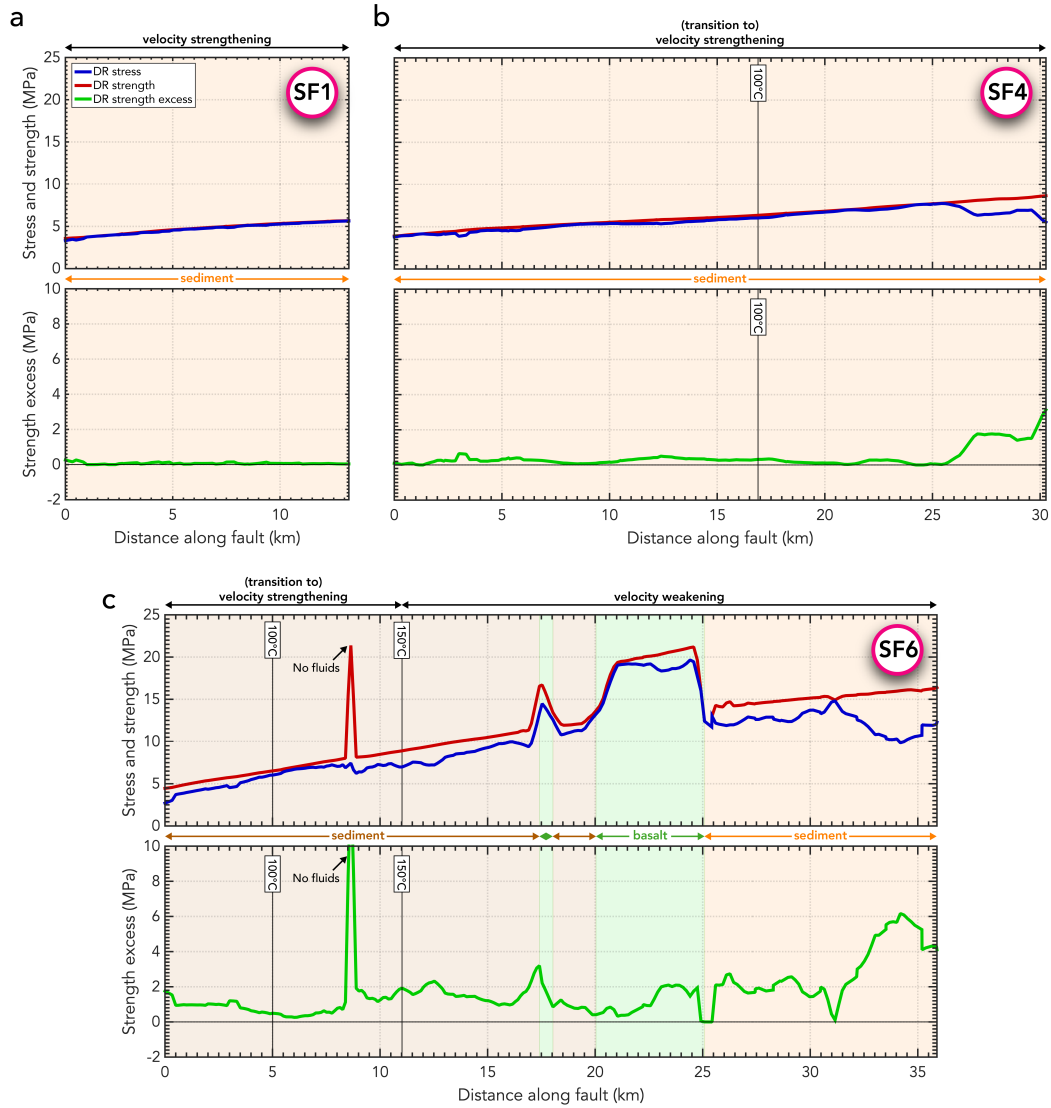


Figure 3. Failure analysis of the initial conditions of the DR model along (a) splay fault 1, (b) splay fault 4, and (c) splay fault 6. See Figures S7-S10 for the failure analysis on the megathrust and the other splay faults. The shallowest part of the fault is at 0; the splay fault connects to the megathrust on the right hand side of the figure. Initial shear stress τ , fault yield stress (strength) $\sigma_{\text{yield}}^{\text{dr}}$, and strength excess $\sigma_{\text{yield}}^{\text{dr}} - \tau$ are shown for the DR model in the fault coordinate system. Frictional regimes dependent on temperature are indicated with corresponding isotherms (solid black lines). Background colours represent the material through which the fault is going: incoming sediments (orange), pre-existing wedge sediments (brown), and basalt (green). Fault strength and therefore stress depends on lithology, which results in stress and strength variations along SF6 that cuts through multiple lithologies. The sharp, localized increase in strength on SF6 is due to a local lack of fluids in the host rock.

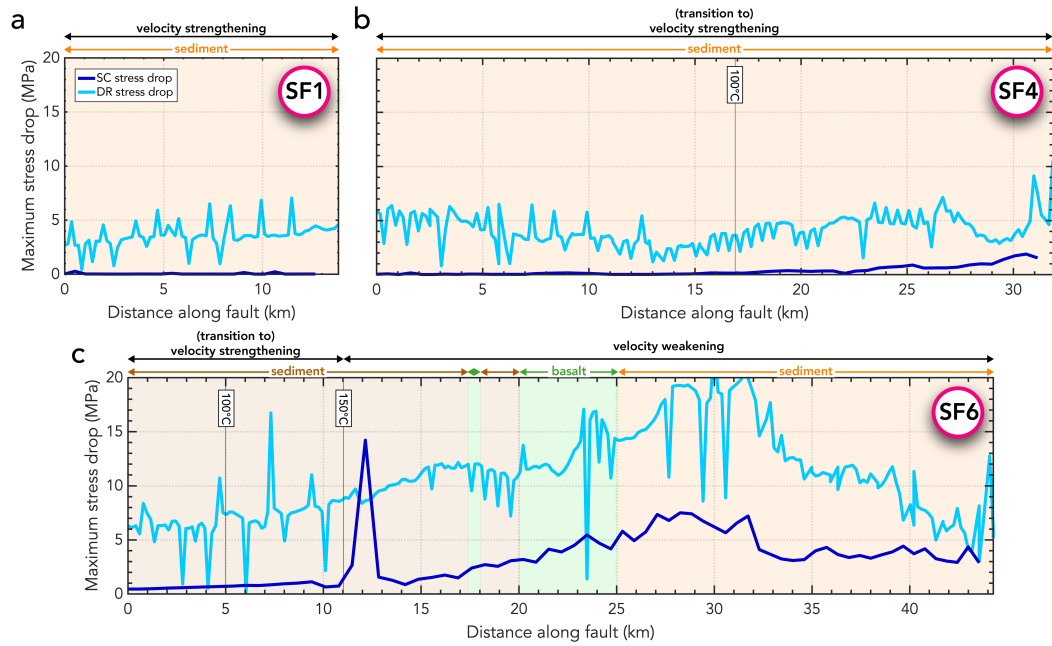


Figure 4. Maximum final stress drop in the geodynamic seismic cycle (SC) and dynamic rupture (DR) models along (a) splay fault 1, (b) splay fault 4, and (c) splay fault 6. See Figures S11-14 for the maximum final stress drop on the megathrust and the other splay faults. The shallowest part of the fault is at 0; the splay fault connects to the megathrust on the right hand side of the figure. Frictional regimes dependent on temperature are indicated with corresponding isotherms (solid black lines). Background colours represent the material through which the fault is going: incoming sediments (orange), pre-existing wedge sediments (brown), and basalt (green).

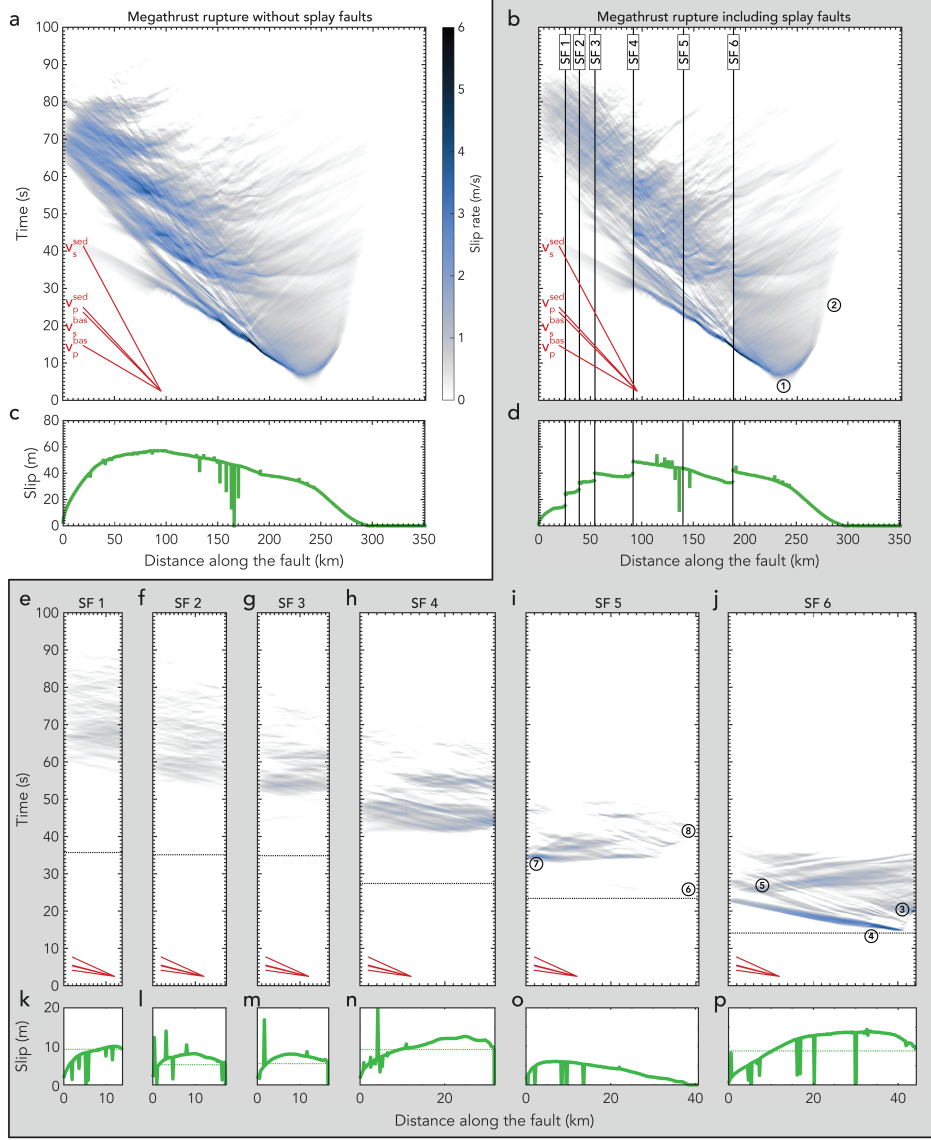


Figure 5. (a,b) Slip rate evolution with time along the megathrust fault for the model (a) without splay faults and (b) including the six splay fault geometries. The splay fault branching points on the megathrust are indicated by black lines. (c,d) Accumulated slip on the megathrust. (e-j) Slip rate evolution and (k-p) accumulated slip on each of the six splay faults for the model including the splay faults. The splay faults connect to the megathrust at the right of each panel. Horizontal black dotted lines indicate the passing of the megathrust rupture front at the branching point. Horizontal green dotted lines in panels k-p indicate the level of local slip deficit at the megathrust at the branching points with each of the splay faults, as measured from the local slip discontinuities in panel d. The P - and S -wave velocities for the basalt and sediment are indicated in red: $v_p^{\text{bas}} = 6164$ m/s, $v_s^{\text{bas}} = 3559$ m/s, $v_p^{\text{sed}} = 4429$ m/s, $v_s^{\text{sed}} = 2557$ m/s. See text for an explanation of the numbers.

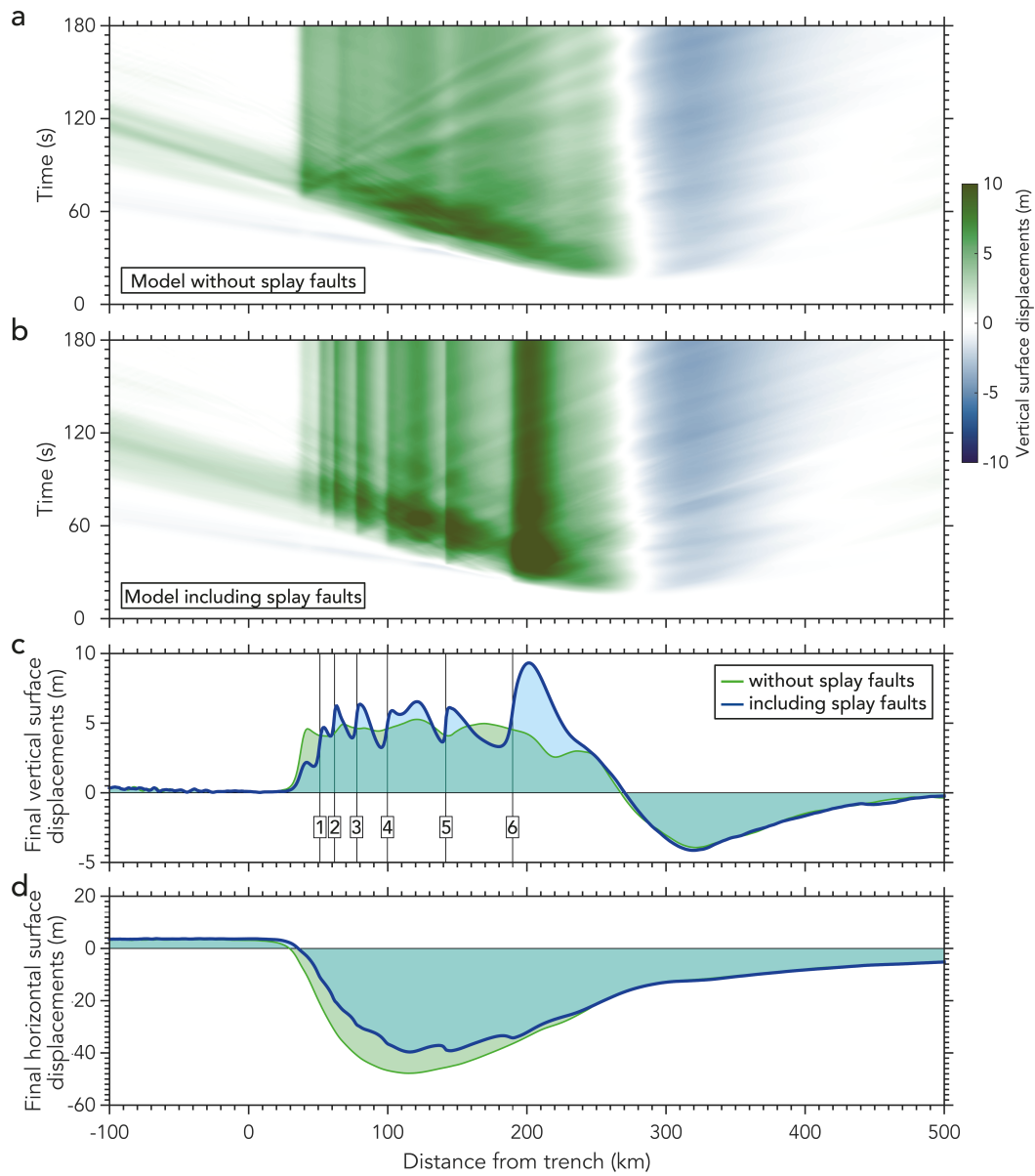


Figure 6. (a,b) Temporal evolution of the vertical surface displacements in the model (a) without splay faults and (b) including all six splay fault geometries. The static vertical (c) and horizontal (d) surface displacements of the two models after 180 s are compared in (c,d) with splay fault numbers indicating the x -coordinates of the shallow splay fault tips near the surface.

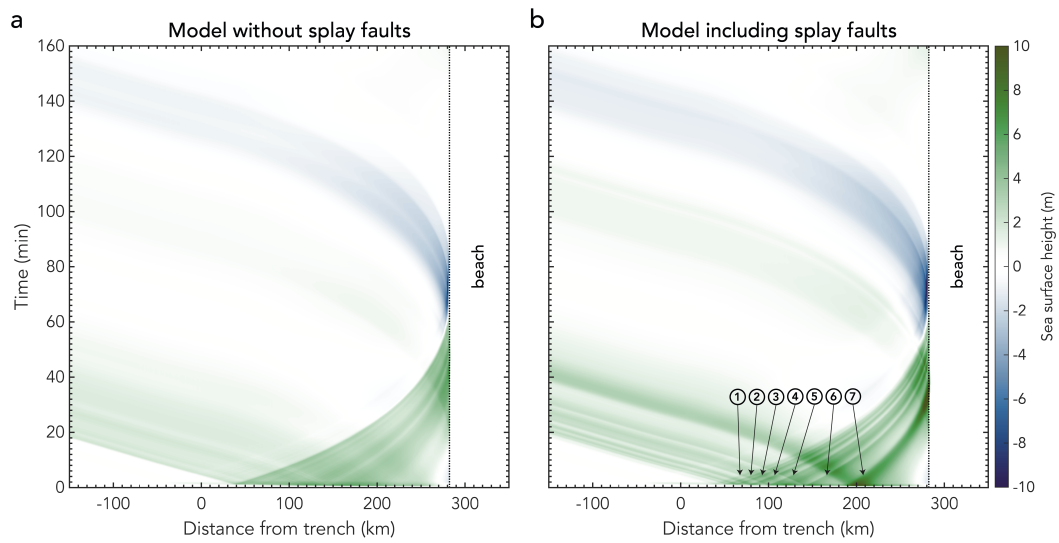


Figure 7. Temporal evolution of the sea surface height for (a) the model without splay faults and (b) the model including all six splay faults.

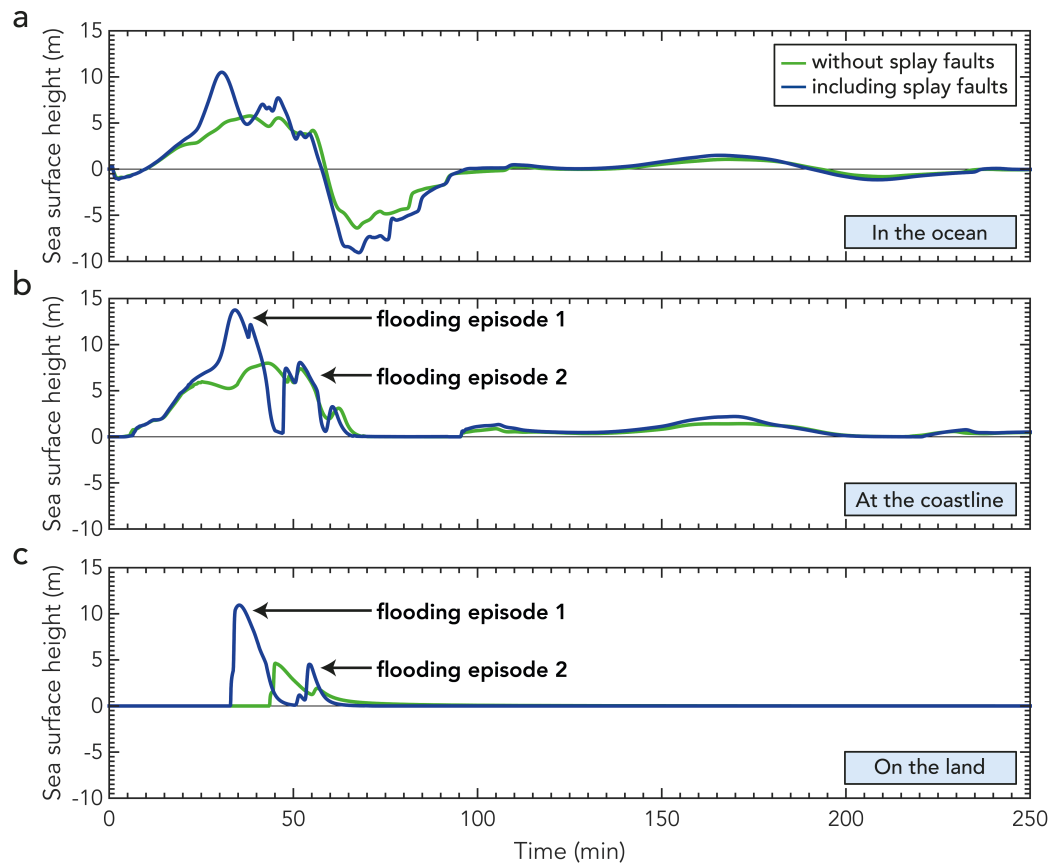


Figure 8. Sea surface height with time at three different locations for both the model without (green) and with (blue) splay faults: (a) $x = 278.46$ km, in the ocean; (b) $x = 282.46$ km, at the coastline; (c) $x = 283.46$ km, on the beach. As the measurements are taken on land in (b,c), the sea surface height should be interpreted as inundation depth.

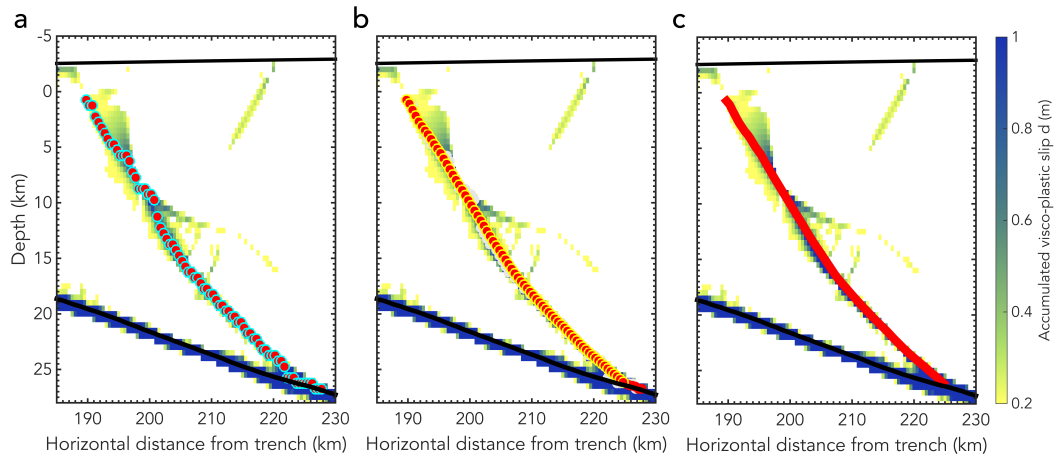


Figure A1. Picking the geometry of splay fault 6. (a) Red dots show the z -coordinate with the highest accumulated strain during the SC event. Red dots with cyan borders show the fault points after the z -coordinate of outliers is corrected. Hence, red dots without a cyan border are interpreted as outliers. (b) Red dots show the smoothed fault geometry after applying a moving average low-pass filter scheme with a span of 25 points. Red dots with yellow borders indicate the eventual selected fault points used to create the mesh. For reference, the red dots with cyan borders of panel (a) are reproduced in grey in the background. (c) Final fault geometry indicated in red. Background colours in panel (a-c) show the final accumulated slip in the sedimentary wedge after the SC slip event. The top black line represents the surface. Bottom thick black line is the megathrust.